Astronomy
&
Astrophysics

A high definition view of the COSMOS Wall at $z \sim 0.73$[★]

A. Iovino[1], V. Petropoulou[1], M. Scodeggio[2], M. Bolzonella[3], G. Zamorani[3], S. Bardelli[3], O. Cucciati[3], L. Pozzetti[3],
L. Tasca[4], D. Vergani[5], E. Zucca[3], A. Finoguenov[6, 7], O. Ilbert[4], M. Tanaka[8], M. Salvato[9], K. Kovač[10], and P. Cassata[11]

[1] INAF–Osservatorio Astronomico di Brera, via Brera, 28, 20159 Milano, Italy
  e-mail: angela.iovino@brera.inaf.it
[2] INAF–IASF Milano, via Bassini 15, 20133, Milano, Italy
[3] INAF–Osservatorio Astronomico di Bologna, via Ranzani 1, 40127 Bologna, Italy
[4] Laboratoire d'Astrophysique de Marseille, CNRS-Université d'Aix-Marseille, 38 rue F. Joliot-Curie, 13388 Marseille, France
[5] INAF–IASF Bologna, via P. Gobetti 101, 40129 Bologna, Italy
[6] Department of Physics, University of Helsinki, G. Hallstromin katu 2a, 00014 Helsinki, Finland
[7] CSST, University of Maryland, Baltimore County, 1000 Hilltop Circle, Baltimore, MD 21250, USA
[8] National Astronomical Observatory of Japan, 2-21-1 Osawa, Mitaka, 181-8588 Tokyo, Japan
[9] Max Planck Institute for Extraterrestrial Physics, Giessenbachstr. 1, 85748 Garching, Germany
[10] Institute of Astronomy, ETH Zurich, 8093 Zürich, Switzerland
[11] Instituto de Fisica y Astronomía, Facultad de Ciencias, Universidad de Valparaíso, Playa Ancha, Valparaíso, Chile

ABSTRACT

Aims. We present a study of a large filamentary structure at $z \sim 0.73$ in the field of the COSMOS survey, the so-called COSMOS Wall. This structure encompasses a comprehensive range of environments from a dense cluster and a number of galaxy groups to filaments, less dense regions, and adjacent voids. It thus provides a valuable laboratory for the accurate mapping of environmental effects on galaxy evolution at a look-back time of ∼6.5 Gyr, when the Universe was roughly half its present age.
Methods. We performed deep spectroscopic observations with VIMOS at VLT of a K-band selected sample of galaxies in this complex structure, building a sample of galaxies complete in galaxy stellar mass down to a lower limit of $\log(\mathcal{M}_*/\mathcal{M}_\odot) \sim 9.8$, which is significantly deeper than previously available data. Thanks to its location within the COSMOS survey, each galaxy benefits from a wealth of ancillary information: HST-ACS data with I-band exposures down to $I_{AB} \sim 28$ complemented by extensive multiwavelength ground- and space-based observations spanning the entire electromagnetic spectrum.
Results. In this paper we detail the survey strategy and weighting scheme adopted to account for the biases introduced by the photometric preselection of our targets. We present our galaxy stellar mass and rest-frame magnitudes estimates together with a group catalog obtained with our new data and their member galaxies color/mass distribution.
Conclusions. Owing to our new sample we can perform a detailed, high definition mapping of the complex COSMOS Wall structure. The sharp environmental information, coupled with high quality spectroscopic information and rich ancillary data available in the COSMOS field, enables a detailed study of galaxy properties as a function of local environment in a redshift slice where environmental effects are important, and in a stellar mass range where mass and environment driven effects are both at work.

Key words. galaxies: evolution – galaxies: groups: general – large-scale structure of Universe

1. Introduction

It is well known that the Universe as a whole formed stars more actively in the past than today. The cosmic star formation rate (SFR) peaks at $z \sim 1$–3 and then decreases by an order of magnitude toward the present day (Madau et al. 1998; Lilly et al. 1996; Hopkins & Beacom 2006; Shioya et al. 2008; Bouwens et al. 2009; Cucciati et al. 2012; Madau & Dickinson 2014). The evolution of the cosmic SFR is an important observational constraint for all the current models of galaxy formation and evolution (Somerville et al. 2012).

Among the different mechanisms that regulate SFR evolution, galaxy stellar mass is a well-known key factor: galaxies of different stellar masses evolve on different timescales according to the so-called downsizing trend (Cowie et al. 1996; Kauffmann et al. 2004).

In the local Universe star formation (SF) activity in galaxies also depends on environment. High density regions, such as groups and clusters of galaxies, are dominated by passively evolving early-type galaxies, while there are many star-forming late-type galaxies in field environments (Dressler 1980; Goto et al. 2003; Bamford et al. 2009). Thus, the fraction of star-forming galaxies systematically decreases with increasing local galaxy density (Gómez et al. 2003; Balogh et al. 2004; Kauffmann et al. 2004; Tanaka et al. 2004). This effect is also observed when splitting the analysis into stellar mass bins (Baldry et al. 2006) and thus removing the effect due to high-mass galaxies segregating in the densest environments (Scodeggio et al. 2009; Bolzonella et al. 2010). It is still a matter of debate how the relation between SF and density evolves with cosmic time and what mechanisms drive this evolution (secular as opposed to nurture driven evolution).

By focusing on star-forming galaxies, it is generally found that environment does not significantly affect the SFR-stellar mass relation (Peng et al. 2010; Koyama et al. 2013; Brough et al. 2013) and this fact, coupled with the environmental

---

[★] Based on observations collected at the European Southern Observatory, Cerro Paranal, Chile, using the Very Large Telescope under program ESO 085.A-0664.

effect on the fraction of star-forming galaxies, has been used to advocate a rapid star formation quenching mechanism to explain a galaxy transition from star forming to passive (Brough et al. 2013). On the other hand, by examining the global galaxy population it has been shown that, since $z \sim 1$, galaxies in groups have been converted more rapidly than the global field population from the blue, star-forming, late-type morphology cloud to the red, quiescent, early-type morphology sequence (Iovino et al. 2010; Kovač et al. 2010; McGee et al. 2011; Peng et al. 2012; Popesso et al. 2015; Guglielmo et al. 2015). In particular, the Popesso et al. (2015) modeling of this trend seems to favor a relatively slow star formation quenching mechanism that takes place on timescales of 1 Gyr or more, while Guglielmo et al. (2015) advocate an accelerated star formation in high-mass haloes to explain the trend.

It has also been argued that the SF-density relation should reverse once we reach the epoch when early-type galaxies formed the bulk of their stars ($z \gtrsim 1.5$). During that phase high density regions should host highly star-forming galaxies, but the observational evidence for this is still debated (see Ziparo et al. 2014; Mei et al. 2015). Thus, defining the role played by environmental processes and pinning down which physical mechanisms play an important evolutionary role in dense regions is not a simple task.

The search for the transition population, that is the galaxies with colors that are intermediate between the blue cloud of star-forming galaxies and the passive sequence of galaxies with negligible present star formation, has been particularly elusive. The search for an environmental dependence on the frequency of such population (Mok et al. 2013; Erfanianfar et al. 2016), a dependence that could provide insights into the timescale of the mechanisms at work and useful constraints for simulations, has been equally elusive.

The Cosmological Evolution Survey (COSMOS) offers a unique opportunity to explore this topic: it contains a very complex structure located at $z \sim 0.73$ and so conspicuous that it was clearly evident in the COSMOS photometric catalog (Scoville et al. 2007b). In an extremely narrow redshift slice, $0.72 \leq z_{spec} \leq 0.74$, there is a rich X-ray detected cluster and a number of groups, some of which are X-ray emitting. These groups are embedded in a filamentary structure extending across ~ 20 Mpc (comoving) within the survey field, and are surrounded by significantly lower density foreground and background regions (see George et al. 2011).

Its location at a look-back time of ~ 6.5 Gyr is at a crucial transition epoch when the color-density relation becomes detectable for galaxies of mass $\log{(\mathcal{M}_*/\mathcal{M}_\odot)} \sim 10.5$, while the morphology-density relation remains undetected (Iovino et al. 2010; Kovač et al. 2010).

Similar depth observations at higher redshifts cannot serve our goals, as at $z \sim 1$ only massive galaxies ($\log{(\mathcal{M}_*/\mathcal{M}_\odot)} \gtrsim 11.0$) are detectable in current redshift survey samples. These galaxies are quite rare because of the exponential cutoff at the high-mass end of the galaxy stellar mass function (Ilbert et al. 2010); they are also more rapidly evolving (Noeske et al. 2007; Thomas et al. 2010; Gilbank et al. 2011). Their intrinsic, mass-dependent evolutionary timescale is shorter than the environmental effects. As a result, red galaxies dominate the galaxy stellar mass function in all environments.

In this paper we present the results of an observational campaign targeting this interesting structure. The goal was to obtain a sample complete in galaxy stellar mass down to $\log{(\mathcal{M}_*/\mathcal{M}_\odot)} \sim 9.8$ within this region of the Universe, doubling the numbers of galaxies already available from previous spectroscopic follow-up in this area (Lilly et al. 2007).

These new spectroscopic data enables us both to extend previous analysis to yet unexplored galaxy stellar mass ranges and to define the environment much more sharply. The new sample we present therefore offers the opportunity for a detailed study of galaxy properties as a function of local environment in a redshift slice where environmental effects have been shown to be important, and in a mass range where mass and environment driven effects are both at work.

A fiducial Λ cold dark matter cosmology model is assumed throughout our paper with $H_0 = 70$ km s^{-1} Mpc^{-1}, $\Omega_m = 0.25$, and $\Omega_\Lambda = 0.75$. All magnitudes are always quoted in the AB system (Oke 1974).

2. The COSMOS Wall at $z \sim 0.73$

COSMOS is a panchromatic imaging and spectroscopic survey of a 1.4×1.4 deg^2 field, which is designed to probe galaxy formation and evolution as a function of cosmic time and large-scale structure environment (Scoville et al. 2007c). The core of the COSMOS survey consists of an HST Treasury Project (Scoville et al. 2007a), but the equatorial location of the COSMOS field has offered the critical advantage of allowing major observatories from both hemispheres to observe this field.

At the very beginning of the COSMOS project, photometric data alone were sufficient to detect a prominent large-scale structure located at $z \sim 0.7$ (Scoville et al. 2007b; Cassata et al. 2007; Guzzo et al. 2007). Nevertheless, the low precision of photometric redshifts limited the detailed exploration of the dependency of local environment on quantities, such as galaxy color or galaxy morphology, with the result that galaxy mass appeared to be the main, if not unique, driver of the observed trends.

Since those initial studies, the ancillary photometric and spectroscopic data available in the COSMOS field have increased significantly. The 30-COSMOS photometric reference catalog, now contains magnitudes measured in 30 bands. These include 2 bands from the Galaxy Evolution Explorer (GALEX), 6 broadbands from the SuprimeCam/Subaru camera, 2 broadbands from MEGACAM at CFHT, 14 medium and narrowbands from SuprimeCam/Subaru, J band from the WFCAM/UKIRT camera, K band from the WIRCAM/CFHT camera, and the 4 IRAC/*Spitzer* channels. These magnitudes were obtained using PSF-matched photometry for all the bands from the u to the K band, measured over an aperture of 3″ diameter at the position of the Subaru i+ band detection, while the corresponding magnitudes in the IRAC bands (3.6, 4.5, 5.6, and 8.0 μm) were obtained following the procedure described in detail in Ilbert et al. (2009). The imaging data are extremely deep, reaching $u \sim 27$, $i+ \sim 26.2$, and $K_s \sim 23.7$ for a 5σ detection in a 3″ diameter aperture (the sensitivities in all bands can be found in Capak et al. 2007; Salvato et al. 2009). Highly accuracy photometric redshifts based on this photometric data set were derived using an improved version of the software *LePhare*, which accounts for the contributions from emission lines[1]. The error in the photometric redshift estimate is as low as $0.007/0.012 \times (1+z)$ for galaxies brighter/fainter than $I_{AB} = 22.5$, respectively (Ilbert et al. 2009). The 30-COSMOS photometric catalog contains 1,500,515 sources in total, and 937 013 sources at $i+ < 26.5$ (Ilbert et al. 2009).

The COSMOS field has also been observed in the far-infrared with the Multiband Photometer for *Spitzer* (MIPS)

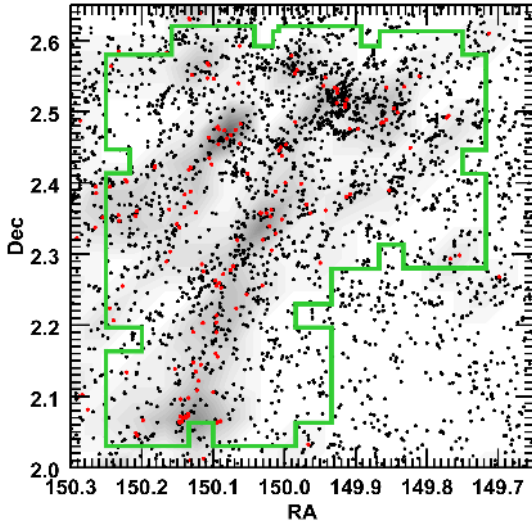[1] See www.oamp.fr/people/arnouts/LE_PHARE.html

Fig. 1. RA-Dec distribution of galaxies within the area we targeted by VIMOS observations, indicated by the green outline. Black dots represent galaxies of the 30-COSMOS photometric catalog with $0.60 \leq z_{phot} \leq 0.86$, while red dots (and the underlying gray contours) represent galaxies from the 20 K-sample in the range $0.72 \leq z_{spec} \leq 0.74$. It is possible to see the presence of a significant galaxy concentration and of two long filamentary structures pointing toward it.

at 24, 70, and 160 μm (Sanders et al. 2007); in the radio continuum with deep 1.4 GHz and 324 MHz observations as part of the VLA-COSMOS survey (Schinnerer et al. 2007; Smolčić et al. 2014); and in the X-ray with both the *XMM-Newton* and the *Chandra* satellites (Hasinger et al. 2007; Elvis et al. 2009), while deep UltraVISTA observations are ongoing (McCracken et al. 2012).

A number of spectroscopic surveys have targeted this field. Publicly available data are provided by the PRIMUS survey (∼30 000 redshifts in the COSMOS field), but with redshift measurement errors that are too large to allow a precise definition of the local environment (Coil et al. 2011). A further public set of redshift measurements is that by Comparat et al. (2015) and was obtained with the FORS2 spectrograph at the ESO Very Large Telescope and targeted color selected emission line galaxies (∼2000 redshift measurements). Finally, the zCOSMOS Bright survey (Lilly et al. 2007), which was carried out with the VIMOS spectrograph at the ESO Very Large Telescope, covers the whole area of the COSMOS field and provides redshifts for ∼20 000 galaxies. These galaxies were selected from a purely magnitude-limited sample down to $I_{AB} \leq 22.5$, as measured from the HST-ACS imaging, with a velocity uncertainty of ∼100 km s^{-1}. This last has been designated as the 20 K-sample (Lilly et al. 2009), and the group catalog derived using these galaxies lists six groups with ten or more spectroscopically confirmed members inside the large-scale structure located at $z \sim 0.73$, thus confirming early photometric results (Knobel et al. 2012).

In Fig. 1 black dots show the distribution on the sky of the 30-COSMOS galaxies brighter than $K_s = 22.6$ and with photometric redshift $0.60 \leq z_{phot} \leq 0.86$. Despite the broad photometric redshift range chosen, a clear concentration of galaxies is visible at the top center of the field, together with two higher density filaments starting from it and extending toward the southeast. The density contrast of the filamentary structures is more striking when considering only galaxies from the 20 K-sample with
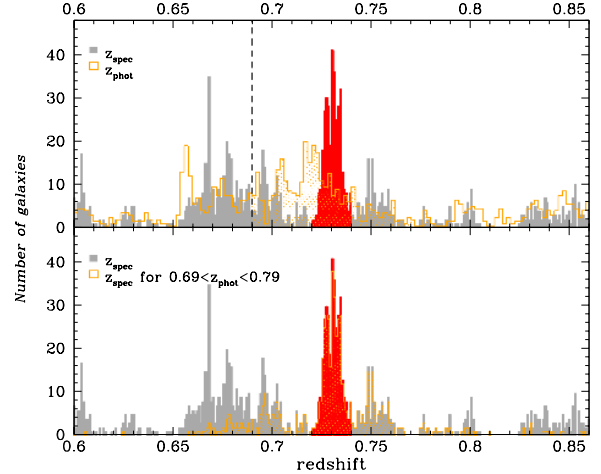

Fig. 2. *Top panel*: redshift histogram of the 20 K-sample within the sky region targeted for observations. In red we highlight the subset of galaxies in the redshift range $0.72 \leq z_{spec} \leq 0.74$, corresponding to the prominent peak of the COSMOS Wall structure. For comparison the orange histogram shows the photometric redshift distribution of the full 20 K-sample within the same sky region. The Wall volume redshift interval, $0.69 \leq z \leq 0.79$ (indicated by two dashed lines), includes both the COSMOS Wall structure and two conspicuous lower density regions in the redshift ranges $0.71 \leq z_{spec} \leq 0.72$ and $0.76 \leq z_{spec} \leq 0.77$. *Bottom panel*: same as top panel but with superimposed (in orange) the histogram of the spectroscopic redshift distribution of the galaxies possessing a photometric redshift within the Wall volume: $0.69 \leq z_{phot} \leq 0.79$.

spectroscopic redshift in the range $0.72 \leq z_{spec} \leq 0.74$, shown as red dots and gray contours in Fig. 1.

In the top panel of Fig. 2 the filled gray histogram shows the spectroscopic redshift distribution of the 20 K-sample galaxies within the sky region highlighted in Fig. 1. In red we highlighted the subset of galaxies in the redshift range $0.72 \leq z_{spec} \leq 0.74$, corresponding to the prominent peak of the COSMOS Wall structure. Adjacent to this high density redshift slice there are two emptier regions in the redshift ranges $0.71 \leq z_{spec} \leq 0.72$ and $0.76 \leq z_{spec} \leq 0.77$, as shown by the dip in numbers of the histogram of Fig. 2.

From now on we call Wall volume the region of volume in space defined in RA-Dec by the polygonal boundaries on the sky shown in Fig. 1, that is the outline of the different VIMOS pointings of our observations (see Sect. 4.1), and defined in redshift by the limits $0.69 \leq z \leq 0.79$. This redshift interval was somewhat arbitrarily chosen to encompass the largest and most prominent groups in the region, and the filaments that connect them, plus the two lower density regions nearby. In this way we can optimally sample a large range of local galaxy densities within a redshift range narrow enough to allow us to neglect evolutionary effects as a function of cosmic time.

In the final 20 K-sample, there are 658 galaxies possessing a reliable spectroscopic redshift within the Wall volume, out of which 350 are within the peak of what we call from now onward the Wall structure, located in the narrow redshift range $0.72 \leq z_{spec} \leq 0.74$ (highlighted in red in Fig. 2). The Comparat et al. (2015) sample contains only 13 additional galaxies within the Wall volume, so, given the complexity of incorporating its different selection criterion in our analysis, we choose to neglect these measurements in the following.
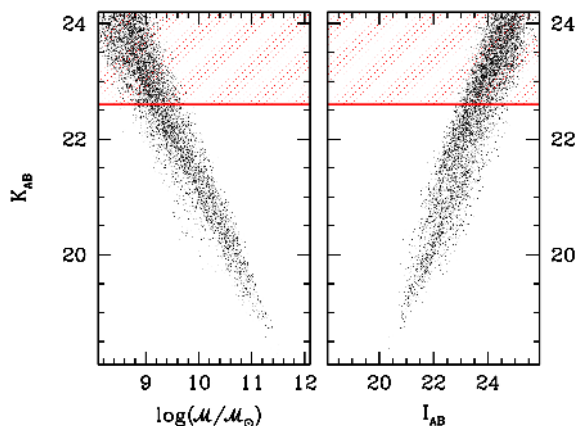
Fig. 3. Both panels: galaxies from the COSMOS photometric catalog with $0.69 \leq z_{phot} \leq 0.79$. *The left panel* shows K_s-band WIRCAM magnitudes versus masses (computed using Chabrier IMF, and Bruzual&Charlot model library, no secondary bursts). The horizontal red line shows our magnitude cut-off $K_s \leq 22.6$, that enables us to reach completeness, irrespective of colors, for masses down to the limit $\log(M_*/M_\odot) = 9.8$. *The right panel* shows K_s-band WIRCAM magnitudes versus I_{AB} magnitudes. Within our K_s-band selection limit the vast majority of galaxies are brighter than $I_{AB} = 24.0$.

3. The enlarged COSMOS Wall sample

We targeted the COSMOS Wall structure with a spectroscopic observational campaign using VIMOS. In the following sections, we describe in detail the magnitude and photometric redshift preselection strategy adopted to optimally define the parent catalog of our observations.

3.1. K-band target selection

An efficient way to select a galaxy sample complete in stellar mass up to $z \sim 1.0$ is to use near-infrared (NIR) K-band photometry. The galaxy emission observed in that band is dominated by the old stellar population that represents the majority of the total stellar mass budget, rather than by the products of the recent star formation activity.

The 30-COSMOS catalog (Ilbert et al. 2009) is providing WIRCAM K_s band aperture magnitudes for galaxies brighter than $K_s \sim 24.0$, together with a rough estimate of the galaxy stellar mass, obtained using the analytical relations from Arnouts et al. (2007). To improve the quality of the stellar mass estimates and for homogeneity with our analysis later on, we decided to recompute these estimates with a full spectral energy distribution (SED) fitting technique, based on an updated version of Hyperzmass (Bolzonella et al. 2000, 2010). The SED templates adopted in this procedure are derived from simple stellar populations (SSPs) modeled by Bruzual & Charlot (2003), adopting the Chabrier (2003) initial mass function (IMF; see for more details Bolzonella et al. 2010).

We then used these stellar mass estimates to check how a K_s-band preselection translates into a galaxy stellar mass selection in the redshift range of interest $0.69 \leq z_{phot} \leq 0.79$. The left panel of Fig. 3 shows that a selection down to $K_s \leq 22.6$ is sufficient to remain complete, irrespective of colors, for galaxy stellar masses down to the limit $\log(M_*/M_\odot) = 9.8$.

The right panel of Fig. 3 shows that the percentage of galaxies at $K_s \leq 22.6$ that are within the photometric redshift range $0.69 \leq z_{phot} \leq 0.79$ and are fainter than $I_{AB} = 24.5$ (well above the 5σ detection limit of the $i+$ Subaru observations), is less than

0.6% and thus negligible. We can therefore be confident that the chosen K_s-band selection limit ($K_s = 22.6$) is well within the range of VIMOS spectrograph capabilities.

3.2. Photometric redshift selection

An important ingredient for our target selection is the use of photometric redshifts to maximize our success rate for galaxies within the Wall volume and minimize observations of interlopers, i.e., galaxies that are outside our redshift range of interest.

The quality of photometric redshifts in the reference 30-COSMOS photometric catalog is very good. Their error is as low as $\sigma \sim 0.007(0.012) \times (1+z)$ down to $I_{AB} = 22.5(24.0)$, respectively (see Ilbert et al. 2009), and we can optimize our target galaxy selection by taking advantage of the available zCOSMOS 20 K-sample spectroscopic redshifts.

A comparison between the capability of the spectroscopic and photometric redshifts in identifying the COSMOS Wall structure is presented the top panel of Fig. 2, where we compare the spectroscopic (in gray and red) and photometric (in orange) redshift distribution of the galaxies in the 20 K-sample located within the RA-Dec outline of the Wall volume (green contours in Fig. 1). The contrast between the Wall structure (red histogram) and the foreground/background distribution is sharper when we use spectroscopic redshifts, although the total number of galaxies selected in the Wall volume changes only slightly when using photometric or spectroscopic redshift values. Intuitively, as many galaxies enter the Wall volume range as many leave owing to uncertainties in photometric redshifts because the main peak of our structure is located far from the selection window limits.

Because of this dilution of contrast it is important to understand how the presence of photometric redshift uncertainties, albeit small, may deteriorate our ability to recover the true spectroscopic redshift distribution within this region when imposing a photometric redshift preselection to the sample targeted for spectroscopic observations.

In the bottom panel of Fig. 2, we overplot on the total spectroscopic redshift distribution already shown in the top panel, the spectroscopic redshift distribution (orange shaded histogram) of the subset of galaxies of the 20 K-sample (645 in total) possessing a photometric redshift in the range $0.69 \leq z_{phot} \leq 0.79$, i.e., within the limits of the Wall volume according their photometric redshift.

It is apparent from this figure that selecting galaxies in the photometric redshift range $0.69 \leq z_{phot} \leq 0.79$ enables us to retrieve ~90% of the 20 K-sample galaxies within the Wall structure (319 galaxies recovered out of 350), and to retrieve ~84% of the full spectroscopic sample within the whole Wall volume (552 galaxies recovered out of 658).

At the same time, only 93 out of the 645, which are selected to have photometric redshift in the range $0.69 \leq z_{phot} \leq 0.79$, are located outside the spectroscopic range $0.69 \leq z_{spec} \leq 0.79$, corresponding to an approximate failure rate of the photometric redshift selection in retrieving the correct spectroscopic redshift sample of ~15%. Obviously, as visible from the bottom panel of Fig. 2, the success rate of the photometric redshift selection has a strong dependence on redshift within our redshift interval of interest. The efficiency in retrieving galaxies located roughly at the center of our photometric selection window is more than 90%, while near the edges of the photometric selection window the efficiency drops to lower values.

We can conclude that a photometric redshift preselection limiting the targets to the photometric redshift range of the Wall volume is efficient in selecting galaxies truly located within the
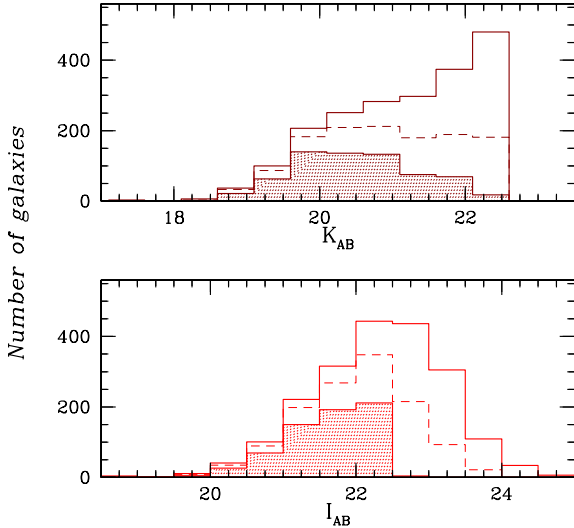
Fig. 4. *Top panel*: K_s-band magnitude distribution of the Wall parent sample. *Bottom panel*: *I*-band magnitude distribution of the Wall parent sample. In both panels the shaded histogram refers to the corresponding magnitude distribution of the subset of galaxies possessing a reliable spectroscopic redshift in the 20 K-sample, while the dashed line to that of our final new Wall volume sample (1277 galaxies).

Fig. 5. Ra–Dec distribution of the 8 VIMOS pointins (P1, P2, ..., P8) of our program. Black dots represent all galaxies of the Wall parent catalog. The large prominent structure on the top north of the field was covered by four pointings.

Wall volume, at least for targets brighter than $I_{AB} = 22.5$. We need to model the loss of efficiency in retrieving the correct redshift selection for targets fainter than $I_{AB} = 22.5$. We discuss in detail in Sect. 6 how to parametrize what we call the photometric redshift efficiency, that is our ability to retrieve the underlying true spectroscopic redshift distribution at all the magnitudes of interest.

4. VIMOS observations

Our observing program was awarded 41 h at the VIMOS multi-object spectrograph, mounted on the Nasmyth focus B of ESO VLT-UT3 Melipal (PI A. IOVINO – ESO 085.A-0664). The VIMOS imaging spectrograph has four channels and each channel (quadrant) covers $7' \times 8'$ with a gap between each quadrant of $\sim 2'$. Each quadrant is a complete spectrograph with the possibility to insert slit masks, as well as broadband filters or grisms, at the entrance focal plane (see Le Fèvre et al. 2003).

3.3. Parent sample definition

The parent sample for our observing program (the Wall parent sample; *WPS*) is then defined by the following conditions:

$$K_s \leq 22.6$$

and

$$0.69 \leq z_{phot} \leq 0.79 \quad \text{or} \quad 0.69 \leq z_{spec} \leq 0.79.$$

It is therefore the full $K_s \leq 22.6$ WIRCAM magnitude limited sample located within the Wall volume, either thanks to spectroscopic redshifts available in the 20 K-sample or to COSMOS photometric redshift information.

Inside the 30-COSMOS catalog there are 2039 galaxies satisfying these constraints, and 658 of these already possess a reliable spectroscopic redshift in the 20 K-sample. In the following we identify the galaxies only possessing a photometric redshift as the WPS_{phot} sample, while the galaxies in the 20 K-sample are identified as the WPS_{spec} sample.

Figure 4 shows the apparent magnitude distribution of the total Wall parent sample in the K_s (top panel) and in the *I* (bottom panel) band. The shaded histograms in both panels refer to the 658 galaxies already possessing a reliable spectroscopic redshift in the 20 K-sample, i.e., those whose location in the Wall volume is already reliably assessed, while the dashed line histogram shows the full set of 1277 galaxies that constitute out new Wall volume sample.
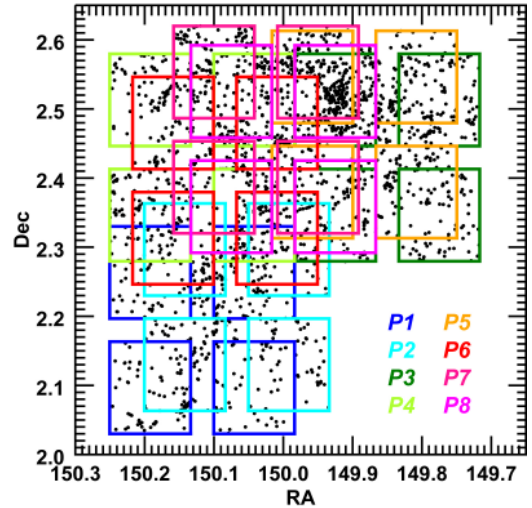
The pixel scale on the $2k \times 4k$ CCD detectors is $0.205''$ pixel^{-1}, providing excellent sampling of the typical image quality at Paranal. The observations were performed during service mode runs in 2010 and 2011. The MR grism and the OS red filter were used, together with $1.0''$ width slits, to produce spectra with a dispersion of 2.5 Å pixel^{-1} covering the spectral range 5550–9450 Å with a spectral resolution $R \sim 600$.

All masks were observed with the slits oriented E-W, thus different from the original N-S orientation adopted by the zCOS-MOS survey. This choice aimed at increasing the homogeneity of the final ra-dec coverage, as the existing WPS_{spec} displayed a slight tendency to be preferentially distributed along N-S stripes (see Lilly et al. 2009)..

All pointings, with the only exception of P1 and P2 (see below), were observed after the VIMOS refurbishing that took place in the Summer 2010 (see below for pointings definition). During the refurbishing the original thinned back-illuminated e2v detectors were replaced by twice as thick e2v detectors, considerably lowering the fringing and increasing the global instrument efficiency by up to a factor 2 for wavelengths longer than 8000 Å (Hammersley et al. 2010). As a consequence, the quality of the spectra obtained with the refurbished VIMOS was significantly better.

The total area covered by our survey amounts to 0.23 deg^2, and the total Wall volume spans a typical transverse dimension of $\sim 21/23$ Mpc at $z \sim 0.69/0.79$ and ~ 300 Mpc along the line of sight, totalling a volume of $\sim 140 \times 10^3$ Mpc^3.

Table 1. Summary of Wall parent sample.

	N_{tot}	WPS$_{spec}$	WPS$_{phot}$
All magnitudes	2039	658	1381
$I_{AB} \leq 22.5$	1143	654	489
$22.5 < I_{AB} \leq 23.0$	436	4	432
$I_{AB} > 23.0$	460	0	460

4.1. Pointing definition strategy

Eight different VIMOS pointings (named P1 to P8) were used to cover the Wall area. In Fig. 5 we show the position of each pointing, together with the position of the galaxies in our parent catalog. We tried to maximize the number of pointings covering the denser regions on the sky while extending the area covered as to include the filamentary distribution of galaxies that defines the COSMOS Wall structure.

The range in I_{AB} magnitudes covered by potential targets in our parent catalog is very wide (see Fig. 4) and we decided to adopt a nonstandard VIMOS observing strategy to obtain spectra with roughly the same quality for all galaxies, while maximizing the number of targets observed.

To obtain spectra with signal-to-noise (S/N) values $\gtrsim 4$ per resolution element we decided to observe the targets brighter than $I_{AB} = 22.5$ for at least roughly one hour, the targets in the magnitude range $22.5 < I_{AB} \leq 23.0$ for roughly two hours, and targets fainter than $I_{AB} = 23.0$ for more than three hours. To achieve this we split the available 3h 37.5m of observing time per each pointing into three modules (or passes) of 1h 12.5m each, so that different galaxies could be observed with different integration times depending on their I_{AB} magnitude.

The number of targets for the various subsets so defined are listed in Table 1. A handful of galaxies in WPS_{spec} that are fainter than $I_{AB} = 22.5$ are secondary targets within 20 K-sample, i.e., targets observed by chance in the slit of a primary target and whose redshift was successfully measured.

Our MOS slit positioning strategy was organized into two steps. Briefly, in the first step we maximized the number of slits positioned on the targets of the WPS_{phot}, i.e., the subset of the Wall parent sample possessing only photometric redshift information. In the second step we added targets from the WPS_{spec} or from the pool of already targeted objects from WPS_{phot} as fillers to our observations, whenever possible, thus increasing their S/N.

The first slit positioning step consisted in allocating in the first pass of each pointing (1h 12.5m exposure time) the maximal number of slits that SPOC, the VIMOS slit positioning software (Bottini et al. 2005), can allocate, starting from the set of objects in the WPS_{phot} sample.

A judicious use of the flags allowed by SPOC (**C** for compulsory, **F** for forbidden, and **S** for observable; see Bottini et al. 2005), then enabled us to force the fainter objects observed in the first pass to be observed in the subsequent passes of each pointing, while new bright objects could be used to replace those already observed in the previous passes. Galaxies with $22.5 < I_{AB} < 23.0$ were observed in at least two passes of 1h 12.5m, totaling 2h 25m of exposure time, while galaxies with $I_{AB} > 23.0$ were observed in all the three passes of the pointing considered, acquiring 3h 37.5m of exposure time.

Once this first step of our observing strategy was consolidated and the list of targets observed in each pass for each pointing is defined according to the rules listed above, we moved to the second phase of our slit positioning strategy. Here we added

to the set of slit targets, defined in the first phase, all possible extra slits that could be positioned either on the galaxies in the WPS_{spec} or on any of the galaxies already targeted in the first step of our slit positioning, thus appreciably increasing the S/N of their spectra.

At the end of this procedure, we were able to position ~130 slits per each pointing on average from the parent catalog. The exact number varies from 150 to 90, depending on the surface target density. The total number of independent targets observed is 1016, all providing extracted spectra for redshift measurements. We positioned 792 slits on targets from WPS_{phot}, while the remaining 224 were positioned on targets from WPS_{spec}, which allows us to significantly improve their spectral quality and provides a set of galaxies useful for defining our accuracy in velocity measurements. Our exposure time for brighter targets is ~20% longer than that of the 20 K-sample observations and the new e2v CCDs, producing significantly improved spectra, were used for most of our observations. We also extract 120 spectra for the secondary targets, which are targets observed by chance in a slit centered on another object. We expect, however, that only a small percentage of this set of objects to be within the Wall volume, as they represent a random sampling of the global galaxy population.

5. Data reduction and redshift measurements

Data reduction for each mask was carried out using the VIPGI software (Scodeggio et al. 2005).

After each CCD frame is bias subtracted, the precise location of the two-dimensional (2D) spectrum for each slit on each frame of the jitter sequence is measured and the position of individual object spectra inside the slit is recorded. The sky background subtraction is carried out for each slit independently, using a two-step procedure. First, the median background level at each wavelength is measured in a single exposure and subtracted from the data; then the median of the sky subtracted spectra is obtained without applying any correction for the telescope pointing offset between exposures. This median produces a frame from which the spectra of individual objects are eliminated, but that includes all residuals not corrected by the first sky subtraction step, and in particular the fringing pattern, which varies with position across the slit and wavelength and is then subtracted from the individual 2D spectra.

The wavelength calibration is obtained via the observation of helium and argon arc lamps through the observed masks, carried out immediately after the sequence of science exposures. Wavelength calibration spectra are extracted at the same location as the object spectra and the lamp lines are identified to derive the pixel to wavelength mapping for each slit. The wavelength to detector pixel transformation is fit using a fourth order polynomial, resulting in a mean rms deviation of ~0.4 Å across the full wavelength range covered by the observations. Finally the sky and fringing residual subtracted and wavelength calibrated 2D spectra are combined together, removing the spectra position offset induced by the jittering pattern, to derive a final combined 2D spectrum for each slit; one-dimensional (1D) spectra are extracted from the combined 2D spectrum, using an optimal extraction procedure, based on the object profile (Horne 1986). Each 1D spectrum is then flux calibrated using the ADU to absolute flux transformation computed from the observations of spectrophotometric standard stars.

Because of the nonstandard observing procedure used for these observations, in which objects are observed repeatedly on different masks, a further data reduction step has to be added to

Table 2. Summary of the observed sample.

	Primary			Secondary
	Observed objects	Successful z	Inside Wall volume	Inside Wall volume
All magnitudes	1016 (224)	975 (224)	836 (224)	20 (13)
$I_{AB} \leq 22.5$	567 (222)	555 (222)	511 (222)	16 (12)
$22.5 < I_{AB} \leq 23.0$	276 (2)	264 (2)	211 (2)	3 (1)
$I_{AB} > 23.0$	173 (0)	156 (0)	114 (0)	1 (0)

Notes. The number in parenthesis always indicates the subset of galaxies from WPS_{spec}. These are targets that are used as fillers in our slit positioning strategy, or, when secondary targets, objects that just enter the slit of a primary target by chance.
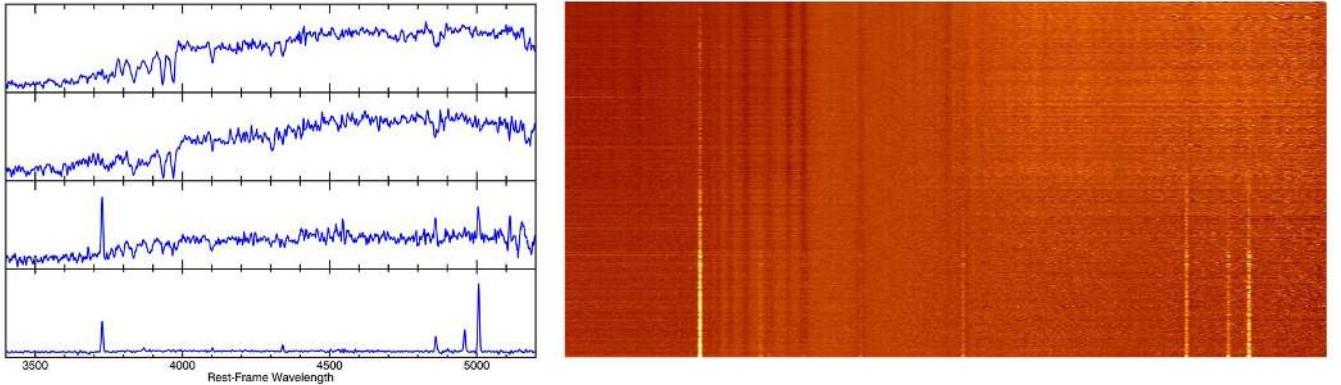

Fig. 6. *Left panel*: examples of our typical spectra, plotted using rest-frame and rebinned to 2 Å pixel^{-1}. *Right panel*: montage of all our rest-frame spectra using the same wavelength range as for the left panel, with galaxy stellar mass decreasing from top to bottom.

the standard VIPGI procedure. For objects with multiple observations, a final combination of all previously obtained 2D spectra is carried out, accounting for the location of the target spectrum. After this final 2D combination, a 1D spectrum is extracted from the combined 2D spectrum and is flux calibrated, following the same VIPGI procedures outlined above.

The redshift measurement is also a multistep process. We start by conducting a fully automated redshift determination based on cross-correlation with template spectra coupled to emission lines and continuum fitting, carried out with the EZ redshift measurement software (Garilli et al. 2010). Galaxy template spectra are drawn from those built for VVDS (Le Fèvre et al. 2005) and zCOSMOS (Lilly et al. 2007) surveys. This automated step is followed by a visual examination of 1D and 2D spectra of every object to assess the validity of the automated redshift measurement, or, if needed, to compute a new redshift, based on the wavelengths of the recognized spectral features. A visual examination is carried out by two people independently, while a third person has the responsibility of establishing the final redshift measurement associated with each spectrum together with a redshift confidence class. These confidence classes are similar to those previously adopted for the VVDS, zCOSMOS, and VIPERS surveys (see Le Fèvre et al. 2005; Lilly et al. 2007; Guzzo et al. 2014), and go from 0 when no reliable spectroscopic redshift measurement is possible, to 4 for a high confidence, highly secure redshift, based on a high S/N spectrum and supported by obvious and consistent spectral features. The statistical meaning of these quality flags is quantified in an objective way in Sect. 5.1, taking advantage of the objects for which redshift is measured twice.

We also add to these integer confidence flags a decimal digit, reflecting an agreement between the spectroscopic and photometric redshift measurement. For objects with $|z_{spec} - z_{phot}|/(1 +$ $z_{spec}) \leq 0.08$, we add 0.5 to the value of the confidence flag, and otherwise we add 0.1. The assumed value of 0.08 corresponds to a conservative estimate for error in photometric redshifts (see Sect. 5.2). Thus, a value of *.5 in this decimal flag improves our confidence in the spectroscopic redshift estimate for a few targets with poor quality spectra.

Table 2 lists, for primary targets of our observations, the numbers of observed objects, the number of successfully measured redshifts (i.e., $z_{flag} \geq 1.5$), and the final number of galaxies observed within the Wall volume, consisting of those galaxies with z_{spec} in the [0.69:0.79] range. The choice of including galaxies with $z_{flag} = 1.5$ in our analysis is justified by the high probability that these redshifts are correct for this redshift confidence class, as estimated in Sect. 5.1.

In the table, we also list a number of secondary targets with reliable redshifts within the Wall volume. As expected, out of a total of 120 secondary targets, for which we were able to measure a reliable redshift, only 20 are inside the Wall volume. The same statistic is also split into three different magnitude ranges. The number in parentheses indicates, for each sample, the subset of targets from the WPS_{spec} sample, which are used as fillers in our slit positioning strategy or, in the case of secondary targets, just enter the slit of a primary target by chance.

Combining our new measurements with the 20 K-sample, we obtain a total sample of 1277 galaxies located within the Wall volume, thus doubling the number of galaxies within the same volume originally available from the 20 K-sample. Out of 1277, 619 are observed during our campaign using the WPS_{phot} sample, 237 are observed during our campaign using the WPS_{spec} sample, and 421 are taken from the 20 K-sample. Hereinafter, we refer to this sample as the COSMOS Wall sample.

On the left panel of Fig. 6 we show some typical spectra. The spectra are all converted to the rest-frame wavelengths, and
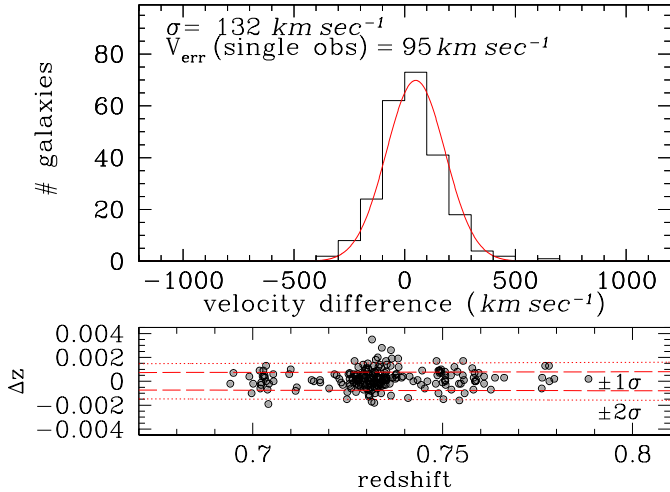
Fig. 7. Our accuracy in the redshift measurements. *Top panel*: histogram of the distribution of velocity differences $\Delta v = c \times \Delta z / (1 + z)$ for the set of 237 galaxies from the $WPS_{\rm spec}$ that were observed twice and whose redshift was independently measured. Such histogram is well fitted by a Gaussian of width $\sigma = 132$ km s^{-1}. *Lower panel*: redshift differences; the dashed (dotted) line corresponds to $\pm 1(2)\sigma$ redshift difference.

rebinned to 2 Å pixel^{-1}. On the right panel we show all our rest-frame spectra, sorted in decreasing galaxy stellar mass from top to bottom. The progressive blueing of the galaxy population moving from higher to lower masses is readily visible, as manifested by the progressive appearance of emission lines.

5.1. Errors in redshift measurements

We estimate a typical accuracy in our redshift measurements taking advantage of the set of 237 galaxies from the 20 K-sample that were reobserved during our campaign.

The top panel of Fig. 7 shows the distribution of the velocity differences between the original 20 K-sample measurements, $\Delta v = c \times \Delta z / (1 + z)$, and ours. Such differences are well represented by a Gaussian of width $\sigma = 132$ km s^{-1}. The lower panel of Fig. 7 shows the redshift differences and the dashed (dotted) line corresponds to $\pm 1 (2) \sigma$ velocity differences. Assuming that the budget in velocity errors is equally distributed between the 20 K-sample and our new data, we infer that the rms of the velocity accuracy of our measurements is ~95 km s^{-1}. In fact, the global velocity uncertainty of 20 K-sample is estimated to be slightly higher, ~110 km s^{-1}; see Lilly et al. (2009). Adopting this value for the contribution of the 20 K-sample to the redshift differences of Fig. 6 results in a lower value for the error budget of our velocity measurements of ~75 km s^{-1}. We adopted a more conservative value of ~90 km s^{-1}, or $\sigma_z = 0.0003 \times (1 + z)$, as an estimate of our error in velocity measurements.

The sample of reobserved galaxies can be further used to quantify the significance of the quality flags introduced in Sect. 5, following the simple strategy adopted in, for example, Le Fèvre et al. (2005) and Guzzo et al. (2014). We make a reasonable assumption that when two measured redshifts are in agreement they are both correct and that two measurements of flag a and b, whose intrinsic probability of being correct is p_a and p_b, respectively, have a probability of being concordant, thus both correct, equal to $p_a \times p_b$.

Out of the 144 pairs of measurements whose assigned flag was 3 or 4, both according to our classification and in the 20 K-sample original spectral classification, no pair has a difference
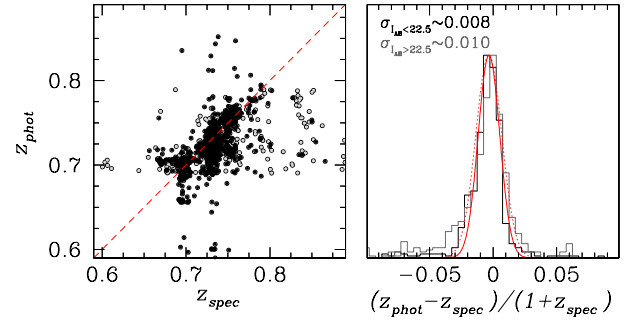
Fig. 8. *Left panel*: $z_{\rm phot}$ vs. $z_{\rm spec}$ for a set of galaxies with $z_{\rm flag} \geq 2$, showing the galaxies brighter/fainter than $I_{\rm AB} = 22.5$ in black/gray. *Right panel*: histogram of $(z_{\rm phot} - z_{\rm spec})/(1 + z_{\rm spec})$ for the same set of galaxies and its Gaussian fit. The black/gray histogram refers to galaxies that are brighter/fainter than $I_{\rm AB} = 22.5$, while the continuous/dotted red line shows the Gaussian fit to the histogram of the brighter/fainter galaxies. The labels indicate the value of σ for each Gaussian.

in redshift measurement greater than $3\sigma_z \sim 0.002$, corresponding to a very high confidence level for this quality class, that is, basically ~100%.

Out of the 45 pairs of measurements where one measurement has flag equal 2 and the other flag equals 3 or 4, only 1 displays a difference greater than $3\sigma_z$, while out of the 13 pairs of measurements whose assigned flags are 2 for both measurements, no pair displayed a difference in redshift measurement greater than $3\sigma_z$. We therefore estimate the confidence level for this quality class as ~98%.

We finally estimate a confidence level for the measurements whose assigned flag is 1.5 (galaxies whose spectroscopic redshift estimate is uncertain, but is backed up by a good agreement with the galaxy photometric redshift). Out of the 20 pairs of measurements, in which one measurement has flag equal to 1.5 and the other flag is equal to 2/3/4, four displayed a difference in redshift measurement greater than $3\sigma_z$, while out of the 3 pairs of measurements whose assigned flag was 1.5 for both, 1 has a difference in spectroscopic redshift measurement between the two estimates that is greater than $3\sigma_z$. Therefore, the confidence level for this quality class can be safely set to ~80%, enough to grant the use of this flag in our subsequent analysis.

5.2. Consistency with photometric redshifts

We use the full sample of galaxies we observed with $z_{\rm flag} \geq 2$ to estimate the typical error of the photometric redshift as a function of target apparent I-band magnitude. This estimate is used in our weighting scheme to account properly for the biases introduced by the photometric preselection of our targets. Using only galaxies with $z_{\rm flag} \geq 3$ does not significantly impact the results, confirming the high reliability of galaxies with $z_{\rm flag} = 2$ (see previous section).

For galaxies at $I_{\rm AB} \leq 22.5$ (black points and red line in Fig. 8) the value of $(z_{\rm phot} - z_{\rm spec})/(1 + z_{\rm spec})$ is well fit by a Gaussian of $\sigma \sim 0.008 \times (1 + z)$, which is in good agreement with Ilbert et al. (2009).

For fainter sample of galaxies at $I_{\rm AB} > 22.5$ (gray points and red dashed line in Fig. 8), the difference between photometric and spectroscopic redshift estimates is well fit by a Gaussian with a slightly higher value of $\sigma \sim 0.010 \times (1 + z)$, which is again in good agreement with the values quoted for similarly faint samples in Ilbert et al. (2009). The fraction of catastrophic

errors (i.e., objects with $|z_{phot} - z_{spec}|/(1 + z_{spec}) > 0.15$) is always $\sim 1\%$ and agrees well with that quoted in Ilbert et al. (2009).

Both for the brighter and fainter sample in the [0.69–0.79] redshift range we detect a small but systematic offset between photometric and spectroscopic redshift values on the order of $(z_{phot} - z_{spec})/(1 + z_{spec}) \sim -0.003$. This effect is visible in the top panel of Fig. 2 as a slight offset between the position of the peak of the COSMOS Wall structure in the spectroscopic or in the photometric redshift distributions.

With our new spectroscopic redshift measurements we can also estimate the net loss of galaxies within the Wall volume due to the use of photometric redshift preselection, both for the brighter subset of galaxies and for the fainter subset.

For brighter galaxies, at $I_{AB} \leq 22.5$, there are 289 galaxies inside the Wall volume out of 333 galaxies with secure redhift from the WPS_{phot} sample, that corresponds to a global success rate of $\sim 86\%$ and is in good agreement with the estimate obtained using the 20 K-sample (see Sect. 3.2).

On the other hand, for fainter galaxies, at $I_{AB} > 22.5$, there are 323 galaxies inside the Wall volume out of 418 galaxies with secure redhift from the WPS_{phot} sample, that corresponds to a lower global success rate of $\sim 77\%$, as expected.

In both cases the exact value of the global success rate is a few percent lower than the value one would naively expect in the presence of catastrophic photometric redshift errors as low as $\sim 1\%$ and perfectly Gaussian statistics. In fact we observe a slightly higher percentage of discrepant objects, with respect to a Gaussian model, whose error in photometric redshift estimate is larger than 3σ and this in turn causes a further lowering of the true global success rate.

6. Correcting for survey incompleteness: weighting scheme

In this section we present a weighting scheme adopted to reconstruct a statistically complete sample starting from our observed Wall sample catalog.

In order to achieve this goal we need to correct for three main factors. First, most of the targets of the parent sample are preselected using photometric redshifts; second, not all the targets of the parent sample are positioned on the slit; and third, we do not succeed in measuring a redshift of every observed object. Our weighting scheme therefore includes three different contributions: the photometric redshift success rate for selection, the target sampling rate, and the spectroscopic success rate. In addition we also introduce a correction to take into account that the target sampling rate is spatially inhomogeneous from the widely varying surface number density of our targets and the finite number of slits per quadrant of each pointing in our observations. Given the negligible number of truly new secondary targets (only seven galaxies are secondary targets that were in the WPS_{phot} sample) in the following, we do not make any distinction in treatment between the primary and secondary targets. In the next sections, we discuss in detail the strategy that we adopt to correct for each of the above-mentioned factors.

6.1. Photometric redshift success rate

The first correction only needs to be applied to the targets selected from WPS_{phot}, which we call it photometric redshift success rate (PhSR).

Targets from WPS_{spec} were selected using their spectroscopic redshift within the 20 K-sample, and thus their selection
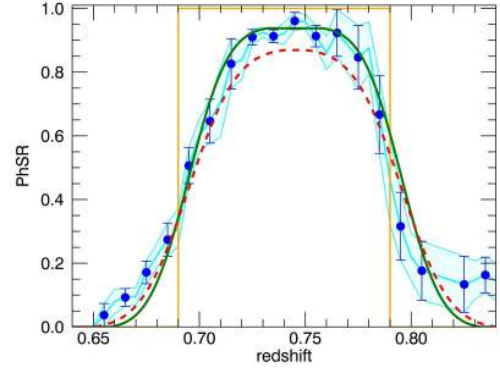

Fig. 9. PhSR as a function of redshift. The top hat function plotted in orange is the selection function holding for WPS_{spec}. The shaded area and blue points refer to the observational estimate (using the 20 K-sample) of the success rate of our photometric redshift selection. The continuous green (dashed red) line shows analytical predictions of PhSR for the sample of targets within WPS_{spec} that are brighter (fainter) than $I_{AB} = 22.5$.

function is well represented by a top hat function with height equal to 1 within the limits $0.69 \leq z \leq 0.79$ and equal to 0 elsewhere, as indicated by the continuous orange line in Fig. 9.

On the contrary, targets from WPS_{phot} were selected using their photometric redshift information. In the bottom panel of Fig. 2 we plot the spectroscopic redshift distribution (orange shaded histogram) for the 20 K-sample galaxies possessing a photometric redshift in the range $0.69 \leq z_{phot} \leq 0.79$, i.e., within the limits of the Wall volume according to their photometric redshift. Clearly we deplete the true spectroscopic redshift distribution within the Wall volume by a factor that increases progressively when moving from the middle of our photometric redshifts selection window toward its edges.

To better visualize this effect in Fig. 9 the blue points and the cyan shaded region show the ratio, as a function of redshift, between the shaded orange and the gray/red histograms shown in the bottom panel of Fig. 2. We consider this an estimate of the success rate of our photometric redshift selection in recovering the actual spectroscopic redshift distribution provided by the 20 K-sample. The blue points are in bins of $\Delta z = 0.01$, while the error bars are obtained using the formula for binomial errors as in Gehrels (1986); the cyan region is obtained with a running bin of width $\Delta z = 0.01$ in steps of $\delta z = 0.005$ and similarly binomial error estimates.

The success rate of the photometric redshift selection (cyan region) has a strong dependence on redshift: it is more than 90% for galaxies at the center of our photometric selection window while it drops to lower values near the edges of the selection window.

Such a dependence can be estimated analytically using the results on photometric redshift errors, as discussed in Sect. 5.2. For targets brighter (fainter) than $I_{AB} = 22.5$ the typical photometric redshift error includes a systematic offset $\delta_{offset} = (z_{phot} - z_{spec})/z_{spec} \sim -0.003 \, (-0.003)$ and a dispersion $\sigma_{photz} \sim 0.008 \, (0.010) \times (1 + z)$, together with a global success rate of $\sim 86 \, (77)\%$ within the Wall volume. We can then analytically parametrize the observed PhSR as a function of redshift by making the convolution of the ideal top hat selection function with a Gaussian of dispersion equal to σ_{photz}, further adding a systematic offset equal to δ_{offset}, and finally renormalizing the integral of the resulting function within the redshift range [0.69–0.79] to
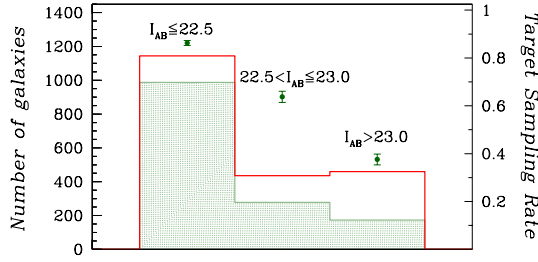
Fig. 10. TSR in the three I_{AB} magnitude bins, used to define our slit positioning strategy: $I_{AB} \leq 22.5$, $22.5 < I_{AB} \leq 23.0$, $I_{AB} > 23.0$. The magnitude bin considered is labeled atop of each bin. The red histogram shows the magnitude distribution of the targets in the total Wall parent sample. The filled green histogram shows the magnitude distribution of the targets where we could position on a slit (for both histograms the corresponding number of targets is shown on the left y axis). The filled points are the TSR, which is ratio between the two histograms, with values given by the right y axis.

the actual value of the global success rate estimated within the Wall volume.

The agreement between the observed and the parametrized PhSR(z) is excellent, as shown by the cyan region and green continuous line in Fig. 9, respectively. We can therefore confidently use this procedure to compute the PhSR analytically both for the brighter and fainter subsets of our targets using the appropriate values for photometric redshift errors as derived in Sect. 5.2. The red dashed line in Fig. 9 shows the results for the fainter subset of our targets.

We adopt these two function as our parametrization of PhSR(z) of brighter/fainter targets from WPS_{phot}, while for targets from WPS_{spec} the PhSR is simply equal to 1. The weight associated with the PhSR is: $w_{PhSR}(z) = 1/PhSR(z)$.

6.2. Target sampling rate

The target sampling rate (TSR) accounts for the selection function of the photometric sources targeted by observations, as we did not position a slit on all the galaxies in the parent sample. The TSR is thus defined as the ratio between the number of photometric sources in the parent sample and the number of photometric sources we targeted with VIMOS observations.

By parent sample, unless specified otherwise, we always mean the total parent sample, that is the sum of WPS_{phot} and WPS_{spec}. Obviously all the objects of WPS_{spec} already possess a spectroscopic redshift from 20 K-sample data so all its galaxies have been *observed* by definition. In the computation of the TSR (and later of the spectroscopic success rate), these objects are treated together with those of the WPS_{phot} to constitute the total parent sample; we consider these among the set of targets where a slit was positioned and a successful redshift was measured. The only difference for the objects of WPS_{spec} is in the treatment of their PhSR, as discussed in the previous section.

As our observing strategy is based on the target I_{AB} magnitude (see Sect. 4.1), we parametrize the TSR as a function of targets I_{AB} magnitude in the three I_{AB} magnitude bins used to define our slit positioning strategy, that is $I_{AB} \leq 22.5$, $22.5 < I_{AB} \leq 23.0$, $I_{AB} > 23.0$.

In Fig. 10 we plot in red the distribution of the number of targets in the parent sample within these three magnitude bins, while the filled green histogram refers to the magnitude distribution of the targets positioned on a slit. The filled points show the ratio between the two histograms, that is the estimate TSR in our three bins of I_{AB} magnitude. The TSR errors are computed
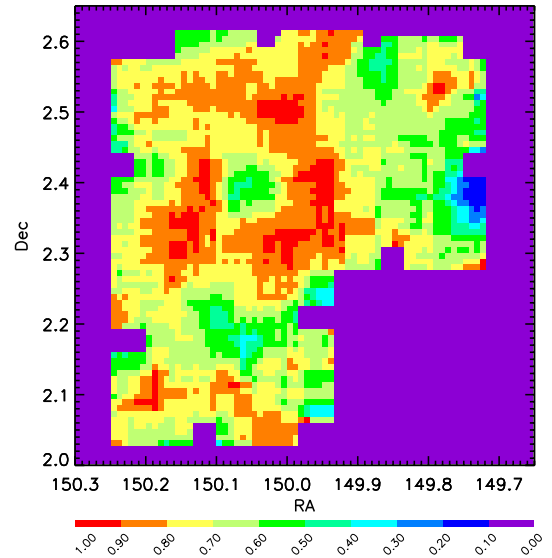

Fig. 11. RaDec Sampling rate before normalization, showing the spatial variation of the TSR due to the sky inhomogeneities in our survey coverage. Comparing this figure with Fig. 5 it is possible to see that the highest density region where the richest structure is located suffers from a slight relative under-sampling, despite having been targeted by four different pointings.

using the formula for binomial errors as in Gehrels (1986). Our average TSR is ∼70%, taking into account the 20 K-sample data. The weight associated with the TSR is $w_{TSR}(I_{AB}) = 1/TSR(I_{AB})$.

6.3. RA-Dec inhomogeneities of TSR

There is a further spatial modulation on the TSR that needs to be taken into account when estimating those physical quantities that depend on the inhomogeneities in our survey coverage. Typical examples of these quantities, such as local densities or group richness estimates.

In this case we need to introduce a RA-Dec sampling rate (RaDecSR), to take into account that the target sampling rate is spatially inhomogeneous owing to widely varying surface number density of our targets and the finite number of slits per quadrant of each pointing in our observations.

To compute RaDecSR we adopt a strategy similar to that one of Iovino et al. (2010), except that we adopt a slightly wider smoothing box size given the lower surface density of our parent catalog. In a grid of steps equal to 30″ in right ascension and declination, and in square cells of $4' \times 4'$, we compute the ratio of the number of targets where a slit is positioned to the total number of parent sample targets within the same area. We then obtain RaDecSR(α, δ) by normalizing to unity the mean value of this ratio over the full RA−Dec coverage of the Wall. The weight associated with RaDecSR is $w_{RaDecSR}(\alpha, \delta) = 1/RaDecSR(\alpha, \delta)$.

In Fig. 11 we show the spatial variation of RaDecSR(α, δ) before normalization; the color scale provides the legend for the range of values shown on the plot. One can appreciate that despite having been targeted with four different pointings, the area where the largest cluster is located still has a relative under-sampling due to the high local density of targets.

6.4. Spectroscopic success rate

Finally, the spectroscopic success rate (SSR) accounts for the fact that not all the sources where we positioned a slit provide a
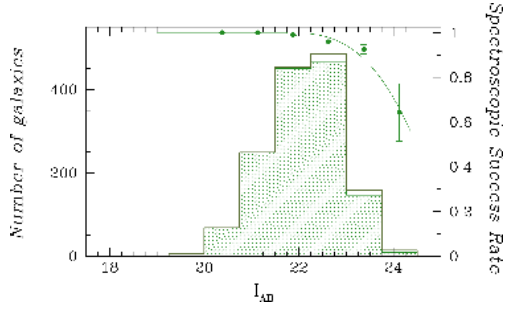
Fig. 12. SSR as a function of a target I_{AB} magnitude. The dark green histogram shows the magnitude distribution of the targets from the total parent sample where a slit was positioned. The filled light green histogram shows the magnitude distribution of the targets whose redshift is reliably measured (for both histograms the numbers are indicated on the left Y axis). The filled points are the SSR, which is a ratio of the two histograms whose value is indicated on the right Y axis. The continuous light green curve is the adopted function to parametrize SSR(I_{AB}).
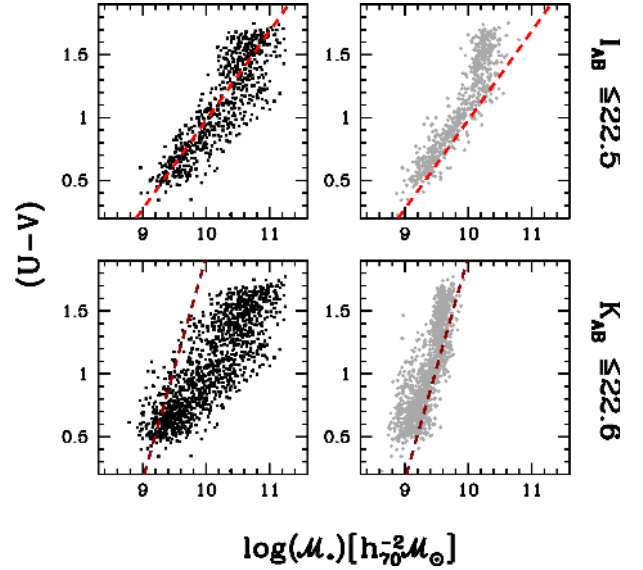

Fig. 13. Stellar mass completeness as a function of galaxy $(U - V)$ rest-frame colors for the whole COSMOS Wall sample limited to $K_{AB} \le 22.6$ (*bottom panel*) and for the subset limited at $I_{AB} \le 22.5$ (*top panel*), which reproduces the completeness of the 20 K-sample. *Left hand panels* display the actual galaxy stellar mass distribution, while *the right hand panels* show the limiting masses for each galaxy, all as a function of $(U - V)$ rest-frame colors, plotted on the y axis. The dashed lines represent the mass limits estimates.

successful redshift measurement. The SSR is thus defined as the ratio between the number of photometric sources where we positioned a slit and the number of reliable redshift measurements obtained. Given the good quality of most of our spectral data, the total SSR is on the order of ~95%, and we adopt a simple parametrization based on the target I_{AB} magnitude, as shown in Fig. 11. A more complex functional form for the SSR, which also includes the rest-frame galaxy colors, is deemed unnecessary (see also Fig. 2 in Lilly et al. (2009), where no significant dependence on the rest-frame galaxy colors for the fraction of spectra yielding a successful redshift measurement is visible at $z \sim 0.7$).

In Fig. 12 the dark-green histogram shows the magnitude distribution of the targets from the total parent sample where a slit was positioned, while the filled light green histogram shows the magnitude distribution of the targets whose redshift was reliably measured (for both histograms numbers are indicated on the left y axis values). The filled points indicate the SSR, computed as a ratio of the two histograms. The continuous light green curve is the function adopted to parametrize SSR(I_{AB}). The weight associated with SSR is $w_{SSR}(I_{AB}) = 1/SSR(I_{AB})$.

For each galaxy i we can thus estimate its total weight using the formula $w_i = w(\alpha_i, \delta_i, z_i, I_{ABi}) = w_{PhSR}(z_i) \times w_{TSR}(I_{AB\,i}) \times w_{RaDecSR}(\alpha_i, \delta_i) \times w_{SSR}(I_{AB\,i})$.

7. Rest-frame magnitudes and stellar masses

The spectroscopic data of the new COSMOS Wall sample of galaxies is matched with the multiwavelength photometric data for each galaxy to derive rest-frame galaxy properties. We then perform SED fitting to obtain luminosities and stellar masses for each galaxy in our sample using an updated version of *Hyperzmass* (Bolzonella et al. 2000, 2010) and a strategy similar to that adopted in Davidzon et al. (2013).

Given a set of synthetic SEDs, *Hyperzmass* fits these models to the multiband photometry for each galaxy and subsequently selects the model that minimizes the χ^2. We compiled a set of synthetic SEDs using simple stellar populations (SSPs) provided by the models of Bruzual & Charlot (2003), adopting the Chabrier (2003) IMF, and assuming a nonevolving stellar metallicity, for which we consider two values: solar ($Z = Z_\odot$) and subsolar ($Z = 0.2 Z_\odot$). We assume an exponentially declining star formation history (SFH), for which $SFR \propto \exp(-t/\tau)$, with the timescale τ ranging from 0.1 to 30 Gyr.

Finally for the galaxy dust content, we implement the Calzetti et al. (2000) and Prevot-Bouchet (Prevot et al. 1984; Bouchet et al. 1985) extinction models, with values of $A(V)$ ranging from 0 (no dust) to 3 mag.

Davidzon et al. (2013) provide for a lengthy discussion of possible alternative choices of codes and spectral library parametrizations and their impact on stellar mass estimates. Here, it is enough to mention that given the wide range of physical properties allowed in the SED fitting procedure, we decided to exclude some unphysical parameter combinations from the fitting. In particular, we limit the amount of dust in passive galaxies (i.e., we impose $A(V) \le 0.6$ for galaxies with $age/\tau > 4$), we avoid very young extremely star-forming galaxies with short τ timescales (i.e., we prevent fits with models with $\tau \le 0.6$ Gyr when requiring $z_{form} < 1$), and we only allow ages to be between 0.1 Gyr and the age of the Universe at the spectroscopic redshift of the fitted galaxy (see Pozzetti et al. 2007; Bolzonella et al. 2010).

We also derive absolute rest-frame magnitudes for each galaxy of the COSMOS Wall sample, using the apparent magnitude that most closely resembles the observed photometric passband, shifted to the redshift of the galaxy under consideration. The k−correction factor in this method is much less sensitive to the adopted SED template type than using a global filter transformation that is confined to a single specific filter passband (see Appendix A of Ilbert et al. 2005).

7.1. Mass completeness of COSMOS Wall sample

As a first test we estimate the stellar mass limits for galaxies of the COSMOS Wall sample. We follow the prescriptions of Pozzetti et al. (2010) to compute for each galaxy its limiting stellar mass, i.e., the stellar mass it would have, at its spectroscopic redshift, if its apparent magnitude is equal to the limiting magnitude of our survey ($K_{AB} = 22.6$). We then use these estimated

limiting masses to define, in bins of $(U - V)$ rest-frame colors, the mass $M^*_{\text{cut−off}}$, below which 85% of limiting masses of galaxies of that color lie. In Fig. 13 we plot these mass limits, together with those of the subset having $I_{AB} \leq 22.5$, to compare our actual gain in mass completeness with respect to the 20 K-sample directly.

In this figure the right panels show the values of these limiting masses while the left panels represent the galaxy stellar mass distribution, both as a function of rest-frame $(U - V)$ colors. The top panels refer to the subset limited to $I_{AB} \leq 22.5$, while the bottom panels correspond to the whole COSMOS Wall sample. The dashed lines represent the mass limits computed as discussed above; the increment in stellar mass depth achieved with respect to the original 20 K-sample is readily appreciable. We confirm that we reached the initial mass limit goal of $\log(\mathcal{M}_*/\mathcal{M}_\odot) = 9.8$ for the reddest galaxies of our sample, thus improving by nearly a decade in mass the original 20 K-sample completeness limit at these redshifts (Pozzetti et al. 2010; Bolzonella et al. 2010; Iovino et al. 2010).

The adopted K_{AB} selection makes the stellar mass limit much less dependent on galaxy colors than an I_{AB} selection; the line that indicates the mass limit in Fig. 13 is significantly less slanted for the K_{AB} selection than for the I_{AB} selection. As a consequence, we can also incorporate in our analysis a significant tail of the I_{AB} bright and blue galaxy population, which is absent in the mass complete subset of the 20 K-sample. This is another way to state that using K_{AB} selection enables us to observe the missing red counterparts of the existing low-mass blue galaxies in the 20 K-sample. Thus, with our survey we double the sample of spectroscopic redshifts available within the Wall volume, but we roughly quadruple the number of galaxies that are used to define a stellar mass complete sample down to our mass limit of $\log(\mathcal{M}_*/\mathcal{M}_\odot) \sim 9.8$. In the 20 K-sample only ~200 out of 658 galaxies in the z-range [0.69−0.79] form a complete sample down to $\log(\mathcal{M}_*/\mathcal{M}_\odot) \geq 10.7$, while in the new COSMOS Wall sample ~800 galaxies form a complete sample down to $\log(\mathcal{M}_*/\mathcal{M}_\odot) \geq 9.8$ out of a total of 1277 galaxies.

A simple sanity check for both our weighting scheme and our stellar mass estimates is obtained by computing the weighted number density of galaxies in bins of galaxy stellar mass, using for each galaxy, the weights discussed in Section 6. Our results can then be compared with those from the survey VIPERS (Guzzo et al. 2014), whose wide area coverage enables a very precise determination of this quantity (Davidzon et al. 2013).

The outcome of this test is shown in Fig. 14. We split the whole COSMOS Wall sample in four galaxy stellar mass bins, as indicated on the top of each panel, and into two redshift ranges: the first corresponding to the Wall structure at $0.72 \leq z \leq 0.74$ (filled red diamonds) and the second to the surrounding foreground and background regions at $0.69 \leq z < 0.72$ and $0.74 < z \leq 0.79$ (empty blue diamonds). The black stars in Fig. 14 are computed using the whole DR1 VIPERS survey data set in the redshift bin $0.69 \leq z \leq 0.79$. Error bars include both Poissonian and cosmic variance contribution except for the points of the Wall structure, where the only error bar shown is the Poissonian one, as we do not claim to be dealing with a representative volume of the Universe; see Driver & Robotham (2010).

While the region of the Wall structure displays a significant overdensity, as expected, with respect to the VIPERS data points, when this region is excised from the analysis, the number densities agree well with those obtained by the VIPERS data set.

In the paper Petropoulou (in prep.), we will present a detailed analysis of the galaxy stellar mass function in the Wall volume, both as a function of environment and of galaxy colors and star
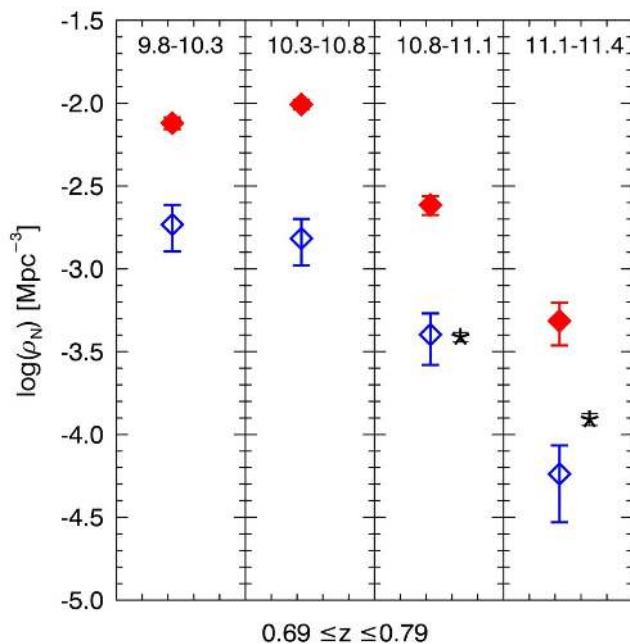

Fig. 14. Number density of galaxies inside and outside the Wall structure indicate red filled diamonds and blue empty diamonds, respectively. The stellar mass bin considered is shown on *the top of each panel*. The black starred points show the number density of galaxies within the same stellar mass bins and in the whole redshift range $0.69 \leq z \leq 0.79$ for the much larger VIPERS survey.

formation properties; this paper will provide a more thorough investigation of this topic.

8. Detection of groups

We targeted the Wall volume because of its interesting large-scale structure: a significant galaxy concentration and two long filamentary structures, embedding groups, extending from it. In the original 20 K-sample group catalog there are 19 (6) groups with 5 (10) or more spectroscopic members within the Wall Volume, and 11 (6) are located within the Wall structure at $0.72 \leq z_{\text{spec}} \leq 0.74$.

With the new data set available we can improve the definition of groups as a result of our better spatial sampling within this interesting region. We use a friend-of-friends (FOF) group detection algorithm, in a similar fashion to Knobel et al. (2012) and Knobel et al. (2009), adopting the same optimization strategy as defined in these papers. The FOF algorithm has three parameters: the comoving linking length as defined by the b parameter, the maximum perpendicular linking length in physical coordinates, L_{max}, and the ratio R between the comoving linking lengths along and perpendicular to the line of sight. Eke et al. (2004) and Knobel et al. (2012) provide a definition of these parameters and a discussion of their optimal values.

The comoving linking length perpendicular to the line of sight, $l_\perp$, is defined as

$$l_\perp = \min[L_{\text{max}}(1 + z),\ b \text{ times } \bar{n}^{-1/3}(z)] \qquad (1)$$

where the free parameter L_{max}, expressed in physical coordinates, prevents unphysically large values for $l_\perp$, when the galaxy distribution is sampled very sparsely and $\bar{n}(z)$, the mean density of galaxies, is low. In our survey the mean intergalactic distance between galaxies $\bar{n}^{-1/3}(z)$ is equal to ~4.8 Mpc in the redshift range $0.715 \leq z \leq 0.775$, while it progressively increases
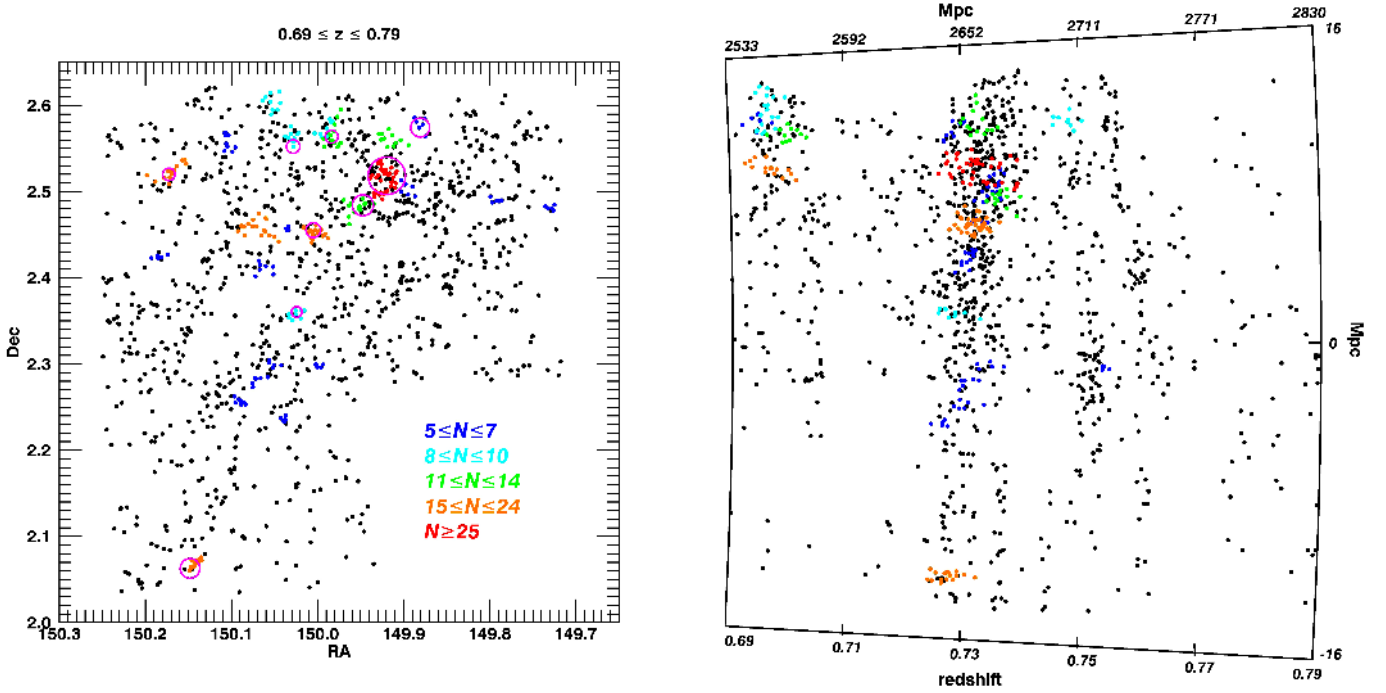
Fig. 15. *Left panel*: RA-Dec distribution of the total Wall sample (black points) and group member galaxies, color coded as indicated in the legend. Large magenta open circles indicate the sky position of the extended X-ray sources from George et al. (2011). *Right panel*: distribution of declination and redshift for the Wall sample and group member galaxies; color legend as in *the left panel*. Labels on the top show distances from observer in comoving coordinates (Mpc units), while labels on the bottom show redshift values. Labels on the right indicate distances in comoving coordinates (Mpc units) from field center along Dec direction at $z \sim 0.79$. For the sake of clarity, in this cone diagram we compressed by a factor 10 the scale along the redshift direction.

on moving away from the central, better sampled region of the Wall volume, reaching the values of ~6.33 Mpc at $z = 0.69$ and ~5.58 Mpc at $z = 0.79$ and following our lower sampling rate in these outer regions (see also Fig. 9).

The comoving linking length parallel to the line of sight, $l_\parallel$, is defined as

$$l_\parallel = R \times l_\perp, \tag{2}$$

where the parameter R allows $l_\parallel$ to be larger than $l_\perp$ to take into account the elongation of groups along the line of sight due to the so-called Fingers of God effect.

Two galaxies i and j, at comoving distances d_i and d_j, are assigned to the same group if their angular separation θ_{ij} satisfies the condition

$$\theta_{ij} \leq \frac{1}{2} \left(\frac{l_{\perp,i}}{d_i} + \frac{l_{\perp,j}}{d_j} \right) \tag{3}$$

and simultaneously, the difference between their distances satisfies the condition

$$|d_i - d_j| \leq \frac{l_{\parallel,i} + l_{\parallel,j}}{2}. \tag{4}$$

We adopt the same multirun procedure as in Knobel et al. (2009, 2012), running the group detection algorithm in different steps optimized for the different observed richness ranges, going from the richest to the poorest groups. In each step only those groups are accepted that have not been found at the previous steps, and the algorithm works down in richness, as the richer groups are more easily detected.

Our choice of parameters follows that in Knobel et al. (2012), as defined after a lengthy optimization procedure, and that paper provides more details. The choice of the multirun

Table 3. Multirun parameter sets for FOF. L_{max} is expressed in physical coordinates.

Step	N_{min}	N_{max}	b	L_{max}	R
1	11	500	0.1	0.375	18.
2	7	10	0.095	0.375	18.
3	6	6	0.09	0.375	17.
4	5	5	0.085	0.35	17.
5	4	4	0.075	0.3	16.
6	3	3	0.07	0.275	16.
7	2	2	0.06	0.225	16.

parameter sets for FOF is listed in Table 3. We detect a total of 57/26/9 groups with 3/5/10 or more observed spectroscopic members within the Wall volume, and 34/19/6 are located within the Wall structure at $0.72 \leq z_{spec} \leq 0.74$.

In Fig. 15, we show the distribution of groups with five or more observed members (color coded according to the number of spectroscopic members; see legend) both in RA-Dec plane and along the redshift direction. Black points refer to the whole Wall sample. Labels on top of the cone diagram represent distances in comoving Mpc, while labels on the right show the size of the corresponding sky region. For the sake of clarity, in the cone shown in the right panel we stretched the scale along the transverse direction by a factor 10.

In Table 4 we list all the groups with five or more observed members sorted according to their observed richness. For each group, we provide its ID; the position in RA and Dec of its center, estimated from the inverse Voronoi area weighted mean of the positions of group members (see Presotto et al. 2012; Knobel et al. 2012); its center in redshift, estimated as the mean redshift of group members; the number of its members

Table 4. Wall volume groups catalog.

ID	Ra (2000)	Dec (2000)	z	N_{obs}	N_{corr}	σ_{gap} (km s^{-1})	$L_{0.1-2.4\ keV}$ (erg s^{-1})	$M_{200}/M_{\odot}$	R_{200} (Mpc)	ID$_{Xray}$	Sep) ($''$)
W1	149.9216	2.5175	0.7307	39	58.1	643	44.052	14.336	0.954	COSMOS CL J095941.6+023129	7.9
W2	150.0684	2.4558	0.7304	20	31.5	322					
W3	150.0036	2.4509	0.7310	20	25.3	299	42.727	13.483	0.495	COSMOS CL J100001.7+022712	17.0
W4	150.1422	2.0684	0.7266	17	23.1	361	43.010	13.667	0.571	COSMOS CL J100035.2+020346	28.8
W5	150.1700	2.5230	0.6967	15	28.2	461	42.583	13.404	0.472	COSMOS CL J100041.4+023124	14.5
W6	149.9807	2.5594	0.7316	14	25.2	323	42.611	13.41	0.469	COSMOS CL J095956.6+023353	19.1
W7	149.9518	2.4819	0.7350	14	19.0	265	43.097	13.72	0.593	COSMOS CL J095946.9+022908	17.9
W8	149.9178	2.5618	0.6999	11	24.7	316					
W9	150.0291	2.5625	0.7471	10	17.4	281	42.647	13.426	0.471	COSMOS CL J100007.9+023308	36.6
W10	149.9890	2.5739	0.6956	9	17.9	238					
W11	150.0518	2.5983	0.6966	9	14.2	230					
W12	150.0294	2.3568	0.7261	9	18.0	386	42.489	13.332	0.442	COSMOS CL J100005.8+022137	23.3
W13	149.8817	2.5764	0.6950	7	19.5	259	42.970	13.654	0.572	COSMOS CL J095930.7+023440	7.9
W14	150.0885	2.2565	0.7280	7	9.3	303					
W15	150.0635	2.4133	0.7292	7	18.5	197					
W16	149.8979	2.5053	0.7350	7	12.5	139					
W17	150.0710	2.2823	0.7288	6	9.2	228					
W18	150.0394	2.2342	0.7251	5	6.7	177					
W19	150.1042	2.5524	0.7264	5	7.0	138					
W20	150.1068	2.5677	0.7292	5	9.7	138					
W21	150.1833	2.4233	0.7302	5	7.7	125					
W22	150.0361	2.4567	0.7319	5	8.1	189					
W23	149.7275	2.4802	0.7329	5	10.1	361					
W24	150.0534	2.2997	0.7331	5	7.9	339					
W25	149.7924	2.4895	0.7338	5	7.2	186					
W26	150.0017	2.2989	0.7523	5	5.7	64					

possessing a spectroscopic redshift N_{obs}; its corrected richness N_{corr}, obtained by weighting each member galaxy with the weighting scheme discussed in Sect. 6; and the group velocity dispersion σ_{gap} estimated using the gapper method (Beers et al. 1990).

As expected there are some non-negligible differences between our group catalog and that presented in Knobel et al. (2012); the increased space density of our galaxy catalog makes our group search more reliable. Some of the Knobel et al. (2012) groups are split into smaller groups in our catalog, while the reverse is less common, in agreement with an expected higher rate of over-merging compared to fragmentation for the 20 K-sample group catalog, as discussed in Knobel et al. (2012).

The most notable case is the one of their group #34 at $z \sim 0.73$ with 19 spectroscopic members. This is the richest group among those listed in Knobel et al. (2012) and is located within the Wall volume. In our catalog this group is split into three smaller groups with four, four, and two members respectively. It is difficult to assess if this could indeed be a case of over fragmentation within our group catalog. We note, however, (see also below) that no detected X-ray emission from George et al. (2011) coincides spatially with the missing group #34 of Knobel et al. (2012) or with the smaller groups into which we have fragmented it.

The largest group we detect, group $W1$ in Table 4 with 39 observed members, can also be found within the Knobel et al. (2012) catalog, albeit in a slightly different configuration. Only 12 of the member galaxies of group $W1$ possessed a

reliable spectroscopic redshift in the 20 K-sample, and 10 were grouped together in group #32 of Knobel et al. (2012).

In general, if we consider a subset of the galaxies in the Wall volume that we deem isolated (i.e., not members of any of our groups, including pairs, triplets, and quartets) and that were observed in the 20 K-sample, only ~15% of these were classified as group members in Knobel et al. (2012). This number further decreases by a factor of two if we consider only those classified in Knobel et al. (2012) as members of groups with multiplicity above 3. Vice versa, if we consider the subset galaxies in the Wall volume classified as members in our whole group catalog, such that at least two group members were observed in the 20 K-sample, nearly all of these (~90%) are classified as group members in Knobel et al. (2012).

As a further check we matched our group list with the published list of XMM-COSMOS extended sources presented in George et al. (2011). We adopted as matching criterion a maximal angular distance on the sky of R_{200} in arcsecs, as estimated from X-ray data and listed in George et al. (2011), and a $\Delta z \sim 0.0035 \times (1 + z)$ in redshift. Out of the nine groups in our catalog with ten or more spectroscopic members, seven are associated with an X-ray detected group in George et al. (2011). Interestingly, the richest group we detect, which is group W1 in Table 4, overlaps with the most luminous and most massive X-ray extended source in George et al. (2011). Large magenta circles on the left panel of Fig. 15 indicate the sky position of these extended X-ray sources (size proportional to the X-ray luminosity).

Vice versa, out of a total of 12 extended sources listed in George et al. (2011) in the redshift range $0.69 \leq z_{\mathrm{spec}} \leq 0.79$ and within our survey area, 9 possess a match with one of our groups while 3 are unmatched. Group W2 in Table 3, however, is roughly 90″ off one of these unmatched extended X-ray sources, COSMOS CL J095908.0+022802, whose R_{200} is ~60″. For this group we may have a centering problem due to our incomplete sampling rate and/or overmerging of two distinct, but adjacent, smaller structures.

For each of our groups possessing a match with those listed in George et al. (2011), we provide the corresponding X-ray information as provided in George et al. (2011) in the last five columns of Table 4: the logarithm of the rest-frame luminosity in the 0.1–2.4 keV band; an estimate of the cluster mass, $\log(M_{200})$, from weak-lensing-calibrated X-ray luminosity vs. cluster mass scaling relation; an estimate of the cluster virial radius, R_{200} in Mpc; the George et al. (2011) cluster ID; the distance in arcsec between the centers of the two matched clusters.

9. Color and mass distribution of groups members

As final sanity check on the quality of our group catalog, we searched for the presence of the well-known interdependencies between environment, galaxy masses, and colors (Bolzonella et al. 2010; Cucciati et al. 2010; Iovino et al. 2010). One of the final goals of our survey is to provide a data set that enables a detailed exploration of the interplay between the environment in which a galaxy resides and its photometric and spectroscopic properties. We choose a selection as close as possible to galaxy stellar mass of the sample observed to enable an analysis down to yet unexplored low galaxy stellar masses.

While such a detailed study is beyond the scope of this paper, we performed a simple analysis of the distribution of stellar masses and $(U-B)$ rest-frame colors dividing the Wall total sample simply into three broad categories. The first includes galaxies located in lower density regions, which consist of either isolated galaxies that are not in any of our detected groups or located in groups with corrected richness $N_{\mathrm{corr}} \leq 4$ and contain 892 galaxies; the second includes galaxies in higher density regions, which encompass those located in groups with corrected richness $4 < N_{\mathrm{corr}} \leq 15$ and include 385 galaxies. Finally, we have a third sample including galaxies in the highest density regions, defined as members of the richest groups at $N_{\mathrm{corr}} > 15$, with a total of 192 galaxies.

In Fig. 16 we show an outcome of this analysis. The top panels show the normalized distributions in $(U - B)$ rest-frame colors (on the left) and in galaxy stellar masses (on the right) of these samples. It is obvious that galaxies located in denser environments progressively possess redder colors and higher masses, thus reproducing the well-known trends that are found in the literature. For a more detailed analysis of the spectrophotometric properties of the COSMOS Wall galaxies as a function of their environment, we refer to Petropoulou (in prep.).

10. Summary and conclusions

We have presented the deep spectroscopic observations performed with VIMOS at VLT of the large filamentary structure at $z \sim 0.73$ in the field of the COSMOS survey, also known as the COSMOS Wall. This structure encompasses a comprehensive range of environments: from a dense cluster and a number of galaxy groups to filaments, less dense regions, and voids; thus this structure is of special interest for studies of environmental effects on galaxy evolution.
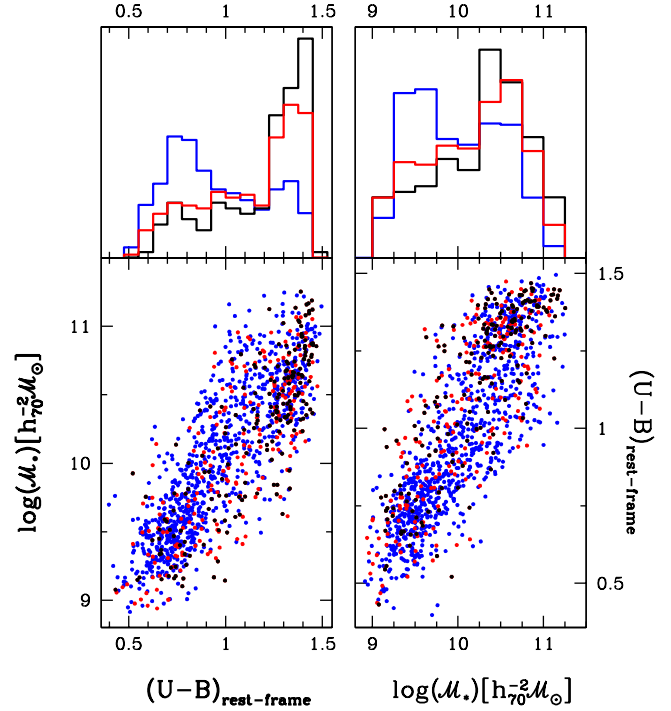

Fig. 16. *Bottom panels*: show the distribution in the plane galaxy stellar mass vs. $(U - B)$ rest-frame color (and vice versa) of all the galaxies of the Wall sample. Each galaxy is color coded according to the environment in which it resides: moving from blue to red and black, galaxies are located in progressively denser environments. *Top panels*: normalized distribution in $(U - B)$ rest-frame colors (*on the left*) and in galaxy stellar masses (on *the right*) of these three samples. Moving from lower to higher densities clearly results both in redder rest-frame color distributions and in stellar mass distributions skewed toward higher masses.

We use photometric redshifts and the K-band selection to target mass-selected galaxies with high probability of being within the volume of interest. This strategy allows us to be very efficient (836 out of the 975 good redshift quality galaxies observed are in the desired narrow redshift range $0.69 \leq z \leq 0.79$) and to reach completeness down to a stellar mass limit of $\log(\mathcal{M}_*/\mathcal{M}_\odot) \sim 9.8$, significantly deeper than previously available data. Thanks to a careful slit positioning strategy we obtained longer exposure times for fainter targets, while retargeting, whenever possible, brighter targets, thus ensuring good quality spectroscopic data.

In this paper we detail the robust weighting scheme adopted to account for the biases introduced by the photometric preselection of our targets and we discuss our final galaxy catalog, together with its physical properties, such as galaxy stellar mass and rest-frame magnitudes estimates.

The final outcome of our survey is a sample of 1277 galaxies within the COSMOS Wall volume, a number that doubles that available in this region from previous surveys. As a result of the deeper galaxy stellar mass limits we reached, we roughly quadruple the number of galaxies within a mass complete sample. In the 20 K-sample only ~200 out of 658 galaxies in the z-range [0.69−0.79] form a complete sample down to $\log(\mathcal{M}_*/\mathcal{M}_\odot) \geq 10.7$, while in the COSMOS Wall sample out of a total of 1277 galaxies, ~800 galaxies form a complete sample down to $\log(\mathcal{M}_*/\mathcal{M}_\odot) \geq 9.8$.

We performed a simple sanity check, for both our weighting scheme and our stellar mass estimates, by computing the number density of galaxies in bins of galaxy stellar mass and comparing this number with results available in the literature. The

agreement is very good: while the region of the Wall structure displays a significant overdensity as expected, when this region is excised from the analysis the number densities as a function of galaxy stellar mass agree well with those in the literature.

Our new sample enables us to perform a detailed, high definition, mapping of the complex Wall structure, and we have built a new group catalog using a FOF algorithm and a multipass procedure. The agreement between the largest groups we detect and the presence of extended X-ray emission from deep published catalogs is remarkable. A simple preliminary exploration of galaxy colors and masses as a function of the environment defined using this groups catalog, reassuringly displays the trends well known in the literature.

The accurate environmental information coupled with good quality spectroscopic information and the rich ancillary data available in the COSMOS field is therefore a gold mine for detailed studies of galaxy properties as a function of local environment in a redshift slice where environmental effects have been shown to be important, and in the mass range where mass and environment driven effects are both at work.

The COSMOS Wall sample presented in this paper thus provides a valuable laboratory for the accurate mapping of environmental effects on galaxy evolution at a look-back time of ~6.5 Gyr, when the Universe was roughly half its present age.

References

Arnouts, S., Walcher, C. J., Le Fèvre, O., et al. 2007, A&A, 476, 137
Baldry, I. K., Balogh, M. L., Bower, R. G., et al. 2006, MNRAS, 373, 469
Balogh, M., Eke, V., Miller, C., et al. 2004, MNRAS, 348, 1355
Bamford, S. P., Nichol, R. C., Baldry, I. K., et al. 2009, MNRAS, 393, 1324
Beers, T., Flynn, K., & Gebhardt, K. 1990, ApJ, 100, 32
Bolzonella, M., Miralles, J.-M., & Pelló, R. 2000, A&A, 363, 476
Bolzonella, M., Kovač, K., Pozzetti, L., et al. 2010, A&A, 524, A76
Bottini, D., Garilli, B., Maccagni, D., et al. 2005, PASP, 117, 996
Bouchet, P., Lequeux, J., Maurice, E., Prevot, L., & Prevot-Burnichon, M. L. 1985, A&A, 149, 330
Bouwens, R. J., Illingworth, G. D., Franx, M., et al. 2009, ApJ, 705, 936
Brough, S., Croom, S., Sharp, R., et al. 2013, MNRAS, 435, 2903
Bruzual, G., & Charlot, S. 2003, MNRAS, 344, 1000
Calzetti, D., Armus, L., Bohlin, R. C., et al. 2000, ApJ, 533, 682
Capak, P., Aussel, H., Ajiki, M., et al. 2007, ApJS, 172, 99
Cassata, P., Guzzo, L., Franceschini, A., et al. 2007, ApJS, 172, 270
Chabrier, G. 2003, ApJ, 586, L133
Coil, A. L., Blanton, M. R., Burles, S. M., et al. 2011, ApJ, 741, 8
Comparat, J., Richard, J., Kneib, J.-P., et al. 2015, A&A, 575, A40
Cowie, L. L., Songaila, A., Hu, E. M., & Cohen, J. G. 1996, AJ, 112, 839
Cucciati, O., Iovino, A., Kovač, K., et al. 2010, A&A, 524, A2
Cucciati, O., Tresse, L., Ilbert, O., et al. 2012, A&A, 539, A31
Davidzon, I., Bolzonella, M., Coupon, J., et al. 2013, A&A, 558, A23
Dressler, A. 1980, ApJ, 236, 351
Driver, S. P., & Robotham, A. S. G. 2010, MNRAS, 407, 2131
Eke, V. R., Baugh, C. M., Cole, S., et al. 2004, MNRAS, 348, 866

Elvis, M., Civano, F., Vignali, C., et al. 2009, ApJS, 184, 158
Erfanianfar, G., Popesso, P., Finoguenov, A., et al. 2016, MNRAS, 455, 2839
Garilli, B., Fumana, M., Franzetti, P., et al. 2010, PASP, 122, 827
Gehrels, N. 1986, ApJ, 303, 336
George, M. R., Leauthaud, A., Bundy, K., et al. 2011, ApJ, 742, 125
Gilbank, D. G., Bower, R. G., Glazebrook, K., et al. 2011, MNRAS, 414, 304
Gómez, P. L., Nichol, R. C., Miller, C. J., et al. 2003, ApJ, 584, 210
Goto, T., Okamura, S., Yagi, M., et al. 2003, PASJ, 55, 739
Guglielmo, V., Poggianti, B. M., Moretti, A., et al. 2015, MNRAS, 450, 2749
Guzzo, L., Cassata, P., Finoguenov, A., et al. 2007, ApJS, 172, 254
Guzzo, L., Scodeggio, M., Garilli, B., et al. 2014, A&A, 566, A108
Hammersley, P., Christensen, L., Dekker, H., et al. 2010, The Messenger, 142, 8
Hasinger, G., Cappelluti, N., Brunner, H., et al. 2007, ApJS, 172, 29
Hopkins, A. M., & Beacom, J. F. 2006, ApJ, 651, 142
Horne, K. 1986, PASP, 98, 609
Ilbert, O., Tresse, L., Zucca, E., et al. 2005, A&A, 439, 863
Ilbert, O., Capak, P., Salvato, M., et al. 2009, ApJ, 690, 1236
Ilbert, O., Salvato, M., Le Floc'h, E., et al. 2010, ApJ, 709, 644
Iovino, A., Cucciati, O., Scodeggio, M., et al. 2010, A&A, 509, A40
Kauffmann, G., White, S. D. M., Heckman, T. M., et al. 2004, MNRAS, 353, 713
Knobel, C., Lilly, S. J., Iovino, A., et al. 2009, ApJ, 697, 1842
Knobel, C., Lilly, S. J., Iovino, A., et al. 2012, ApJ, 753, 121
Kovač, K., Lilly, S. J., Knobel, C., et al. 2010, ApJ, 718, 86
Koyama, Y., Kodama, T., Tadaki, K.-I., et al. 2013, MNRAS, 428, 1551
Le Fèvre, O., Saisse, M., Mancini, D., et al. 2003, in Instrument Design and Performance for Optical/Infrared Ground-based Telescopes, eds. M. Iye, & A. F. M. Moorwood, SPIE Conf. Ser., 4841, 1670
Le Fèvre, O., Vettolani, G., Garilli, B., et al. 2005, A&A, 439, 845
Lilly, S. J., Le Fevre, O., Hammer, F., & Crampton, D. 1996, ApJ, 460, L1
Lilly, S. J., Le Fèvre, O., Renzini, A., et al. 2007, ApJS, 172, 70
Lilly, S. J., Le Brun, V., Maier, C., et al. 2009, ApJS, 184, 218
Madau, P., & Dickinson, M. 2014, ARA&A, 52, 415
Madau, P., Pozzetti, L., & Dickinson, M. 1998, ApJ, 498, 106
McCracken, H. J., Milvang-Jensen, B., Dunlop, J., et al. 2012, A&A, 544, A156
McGee, S. L., Balogh, M. L., Wilman, D. J., et al. 2011, MNRAS, 413, 996
Mei, S., Scarlata, C., Pentericci, L., et al. 2015, ApJ, 804, 117
Mok, A., Balogh, M. L., McGee, S. L., et al. 2013, MNRAS, 431, 1090
Noeske, K. G., Faber, S. M., Weiner, B. J., et al. 2007, ApJ, 660, L47
Oke, J. B. 1974, ApJS, 27, 21
Peng, Y.-J., Lilly, S. J., Kovač, K., et al. 2010, ApJ, 721, 193
Peng, Y.-J., Lilly, S. J., Renzini, A., & Carollo, M. 2012, ApJ, 757, 4
Popesso, P., Biviano, A., Finoguenov, A., et al. 2015, A&A, 574, A105
Pozzetti, L., Bolzonella, M., Lamareille, F., et al. 2007, A&A, 474, 443
Pozzetti, L., Bolzonella, M., Zucca, E., et al. 2010, A&A, 523, A13
Presotto, V., Iovino, A., Scodeggio, M., et al. 2012, A&A, 539, A55
Prevot, M. L., Lequeux, J., Prevot, L., Maurice, E., & Rocca-Volmerange, B. 1984, A&A, 132, 389
Salvato, M., Hasinger, G., Ilbert, O., et al. 2009, ApJ, 690, 1250
Sanders, D. B., Salvato, M., Aussel, H., et al. 2007, ApJS, 172, 86
Schinnerer, E., Smolčić, V., Carilli, C. L., et al. 2007, ApJS, 172, 46
Scodeggio, M., Franzetti, P., Garilli, B., et al. 2005, PASP, 117, 1284
Scodeggio, M., Vergani, D., Cucciati, O., et al. 2009, A&A, 501, 21
Scoville, N., Abraham, R. G., Aussel, H., et al. 2007a, ApJS, 172, 38
Scoville, N., Aussel, H., Benson, A., et al. 2007b, ApJS, 172, 150
Scoville, N., Aussel, H., Brusa, M., et al. 2007c, ApJS, 172, 1
Shioya, Y., Taniguchi, Y., Sasaki, S. S., et al. 2008, ApJS, 175, 128
Smolčić, V., Ciliegi, P., Jelić, V., et al. 2014, MNRAS, 443, 2590
Somerville, R. S., Gilmore, R. C., Primack, J. R., & Domínguez, A. 2012, MNRAS, 423, 1992
Tanaka, M., Goto, T., Okamura, S., Shimasaku, K., & Brinkmann, J. 2004, AJ, 128, 2677
Thomas, D., Maraston, C., Schawinski, K., Sarzi, M., & Silk, J. 2010, MNRAS, 404, 1775
Ziparo, F., Popesso, P., Finoguenov, A., et al. 2014, MNRAS, 437, 458